

# JGR Solid Earth

## RESEARCH ARTICLE

10.1029/2023JB026957

### Key Points:

- We evaluated the performance of a range of surface wave methods on distributed acoustic sensing (DAS) ambient noise dispersion imaging in an urban area
- We developed a quality control workflow to attenuate the nonuniform source effects on the DAS ambient noise data
- We utilized ambient noise records and local earthquake events observed on DAS for high-resolution site effect estimation

### Supporting Information:

Supporting Information may be found in the online version of this article.

### Correspondence to:

F. Cheng and J. B. Ajo-Franklin,  
fengcheng@zju.edu.cn;  
ra62@rice.edu

### Citation:

Cheng, F., Ajo-Franklin, J. B., & Rodriguez Tribaldos, V. (2023). High-resolution near-surface imaging at the basin scale using dark fiber and distributed acoustic sensing: Toward site effect estimation in urban environments. *Journal of Geophysical Research: Solid Earth*, 128, e2023JB026957. <https://doi.org/10.1029/2023JB026957>




Received 21 APR 2023  
Accepted 10 AUG 2023

### Author Contributions:

**Conceptualization:** Feng Cheng  
**Data curation:** Veronica Rodriguez Tribaldos  
**Formal analysis:** Feng Cheng  
**Funding acquisition:** Jonathan B. Ajo-Franklin  
**Investigation:** Feng Cheng  
**Methodology:** Feng Cheng  
**Project Administration:** Jonathan B. Ajo-Franklin  
**Software:** Feng Cheng  
**Supervision:** Feng Cheng, Jonathan B. Ajo-Franklin  
**Validation:** Feng Cheng  
**Visualization:** Feng Cheng  
**Writing – original draft:** Feng Cheng

© 2023. American Geophysical Union.  
All Rights Reserved.

## High-Resolution Near-Surface Imaging at the Basin Scale Using Dark Fiber and Distributed Acoustic Sensing: Toward Site Effect Estimation in Urban Environments

Feng Cheng<sup>1,2</sup> , Jonathan B. Ajo-Franklin<sup>2,3</sup> , and Veronica Rodriguez Tribaldos<sup>3</sup> 

<sup>1</sup>School of Earth Sciences, Zhejiang University, Hangzhou, China, <sup>2</sup>Department of Earth, Environmental, and Planetary Sciences, Rice University, Houston, TX, USA, <sup>3</sup>Lawrence Berkeley National Laboratory, Berkeley, CA, USA

**Abstract** Near-surface seismic structure, particularly the shear wave velocity ( $V_s$ ), can strongly affect local site response, and should be accurately estimated for ground motion prediction during seismic hazard assessment. The Imperial Valley (California), occupying the southern end of the Salton Trough, is a seismically active basin with thick surficial lacustrine sedimentary deposits. In this study, we utilize ambient noise records and local earthquake events for high-resolution near-surface characterization and site effect estimation with an unlit fiber-optic telecommunication infrastructure (dark fiber) in Imperial Valley by using the distributed acoustic sensing (DAS) technique. We apply ambient noise interferometry to retrieve coherent surface waves from DAS records, and evaluate performances of three different surface wave methods on DAS ambient noise dispersion imaging. We develop a quality control workflow to improve the dispersion measurement of noisy portions of the DAS data set by using a data selection strategy. Using the joint inversion of both the fundamental mode and higher overtones of Rayleigh waves, a high resolution two-dimensional (2D)  $V_s$  structure down to 70 m depth is obtained. We successfully achieve an improved  $V_{s,30}$  (the time-averaged shear-wave velocity in the top 30 m) model with higher spatial-resolution and reliability compared to the existing community model for the area. We also explore the potential for utilizing DAS earthquake events for site amplification estimation. The preliminary results reveal a clear anti-correlation between the approximated site response and the  $V_{s,30}$  profile. Our results indicate the potential utility of DAS deployed on dark fiber for near-surface characterization in appropriate contexts.

**Plain Language Summary** Site effects play a critical role in earthquake ground motions. During an earthquake, the soft sedimentary basin can strongly amplify both the amplitudes and duration of ground motion. Earthquakes are a common occurrence across the soft and thick Imperial Valley Basin in Southern California, where they have been observed for more than two decades. Therefore, the engineering seismology community urgently needs cost-effective and reliable approaches to evaluate the high-resolution site effect across the densely populated Imperial Valley Basin. We utilize a ~28 km-long existing unused telecommunication fiber as an array of seismic sensors using a new sensing technology called distributed acoustic sensing (DAS) to characterize the near-surface structure as well as site response. Our results reveal a high-resolution soil profile of the time-averaged shear-wave velocity in the top 30 m of the basin using DAS ambient noise data, and an approximated site response profile using DAS earthquake events. A clear correlation has been observed between the soil velocity profile and the site response profile from two independent data sets, which corroborates the accuracy of DAS seismic observations and indicates that DAS is a promising tool for high-resolution near-surface site effect estimation as well as seismic hazard mapping.

## 1. Introduction

Thick soft sedimentary deposits can strongly amplify earthquake ground motion (Aki, 1993). This phenomenon is known as the site effect, and depends on the near-surface material properties of the site, such as seismic velocity structure, and geometrical effects, such as surface topography. Near-surface site effect is one of the most influential factors that affect ground motion parameters for engineering design and seismic hazard prevention (Kawase, 1996). During an earthquake, site effects can dramatically increase both the amplitude and duration of ground motion at certain frequencies, particularly for sites located on thick sedimentary deposits (sedimentary valley or basin) like the Imperial Valley. Moreover, seismic waves resonate in three-dimensional (3D) sedimentary

Writing – review & editing: Feng Cheng, Jonathan B. Ajo-Franklin, Veronica Rodriguez Tribaldos

basins and lead to rapid lateral changes of site effects or ground motions over distances of only a few tens of meters (Anderson, 2007; Castellanos et al., 2020; R. Clayton et al., 2019; Imtiaz et al., 2018; Svay et al., 2017).

In recent decades, a variety of methods have been developed to estimate site effects. Borchardt (1970) introduced the standard spectral ratio (SSR) technique to estimate the site response, which is defined as the spectral ratio of an observed earthquake in a sedimentary site with respect to a bedrock reference site (Kagami et al., 1982, 1986; Perron et al., 2018). Unlike techniques that require earthquake observations, Nakamura (1989, 2019) explored the applicability of the horizontal-to-vertical spectral ratio (HVSr) method to estimate dynamic ground response characteristics by using microtremor. Another more straightforward proxy used in site response analysis are local soil profiles, such as the shear-wave velocity ( $V_s$ ) profile (Wills & Clahan, 2006; Xia et al., 1999). The time-averaged shear-wave velocity in the top 30 m (referred to as  $V_{s,30}$ ) of the soil profile has been frequently used in various geotechnical and seismological applications, such as site classification of the National Earthquake Hazards Program (NEHRP) (Dobry et al., 2000).

Local  $V_s$  profiles are usually determined from boreholes (Garofalo et al., 2016; S. Lin & Ashlock, 2014), in situ tests (C. R. Clayton, 1995), or geophysical survey methods, for example, spectral analysis of surface waves—SASW (Nazarian et al., 1983; Stokoe & Nazarian, 1983); multichannel analysis of surface waves—MASW (Foti et al., 2018; C. B. Park et al., 1999; Socco et al., 2010; Song et al., 1989; Xia et al., 1999); refraction microtremor—ReMi (Louie, 2001; Louie et al., 2021; Pancha et al., 2008), roadside passive multichannel analysis of surface wave-PMASW (C. B. Park & Miller, 2008; C. Park et al., 2004), spatial autocorrelation-SPAC (Aki, 1965; Chávez-García et al., 2006; Hayashi et al., 2022; Kita et al., 2011; Margaryan et al., 2009; Okada & Suto, 2003), multichannel analysis of passive surface waves-MAPS (Chen et al., 2022; Cheng et al., 2016; Dai et al., 2021; Y. Liu et al., 2020; Mi et al., 2022; Pang et al., 2019; Zhou et al., 2018). In the past two decades, the ambient noise interferometry technique has been widely employed for subsurface structure imaging using ambient seismic energy from natural or anthropogenic sources (e.g., Lehujeur et al., 2016; Lepore & Grad, 2020; F.-C. Lin et al., 2009; Martins et al., 2020; Nakata et al., 2011; Pan et al., 2016; Planès et al., 2020; Yao & van der Hilst, 2009). Campillo and Paul (2003) indicated that one can extract the empirical Green's function between two receivers by cross-correlating their ambient seismic noise recordings. This work leads a path for non-destructive, efficient and economical seismic imaging and monitoring (Behm et al., 2019; Bensen et al., 2007; Castellanos et al., 2020; James et al., 2019; Mao et al., 2022; Nakata & Snieder, 2014; Nakata et al., 2015; Shapiro & Campillo, 2004; Snieder, 2004; Snieder et al., 2009; Wapenaar, 2004).

With the rapid development of dense nodal array observation techniques in the past decade, special attention has been paid to the use of ambient noise interferometry for high-resolution seismic imaging (Behm et al., 2019; Castellanos & Clayton, 2021; Nakata et al., 2015). However, one demanding challenge for near-surface seismic imaging is to reasonably extend the high-resolution imaging techniques from small scale to large scale with limited budget and resources. Distributed acoustic sensing (DAS) repurposes fiber-optic cables as dense arrays of seismic sensors, which is dramatically changing seismic acquisition, particularly in cases where dense array spacing is required (Cheng et al., 2023a; Daley et al., 2013; Jousset et al., 2022; Walter et al., 2020; Zhan, 2020). The distributed sensing property of DAS yields the unique advantage of satisfying demands of both high spatial-resolution and large spatial-coverage for near-surface seismic imaging. Recently, DAS ambient noise interferometry has been implemented for seismic imaging in various environments and at various scales (Ajo-Franklin et al., 2019; Cheng et al., 2023a; Dou et al., 2017; Fang et al., 2020; Spica et al., 2020b; Zhu et al., 2021).

The Imperial Valley, south of the Salton Sea in southern California, is a tectonically active sedimentary basin (Kaspereit et al., 2016). Earthquakes, including swarms, are a common occurrence near the Salton Sea, where they have been observed for more than two decades (Hauksson et al., 2013; Johnson & Hadley, 1976; Lohman & McGuire, 2007; Wei et al., 2015). The small dots shown in Figure 1 represent historical earthquakes from the catalog relocated by Hauksson et al. (2012). The sedimentary fill has a depth of approximately 5 km in the depocenter and consists of heterogeneous deltaic deposits (Muffler & White, 1969; Winker, 1987). Therefore, accurate knowledge of the site effect of the shallow soft sediment is significant for the community infrastructure and buildings in valleys located in or near tectonically active areas.

In this study, we investigate the possibility of using DAS data acquired on existing unused telecommunications fiber (~28 km) for high-resolution site effect estimation across the Imperial Valley basin. The data set provides an excellent opportunity to investigate site response and near-surface structure in a region with a history of strong ground motion and significant earthquake hazards. We retrieve high-quality Rayleigh waves from anthropogenic noise using ambient noise interferometry and generate a shallow (~70 m) high-resolution 2D  $V_s$  model using surface wave inversion.

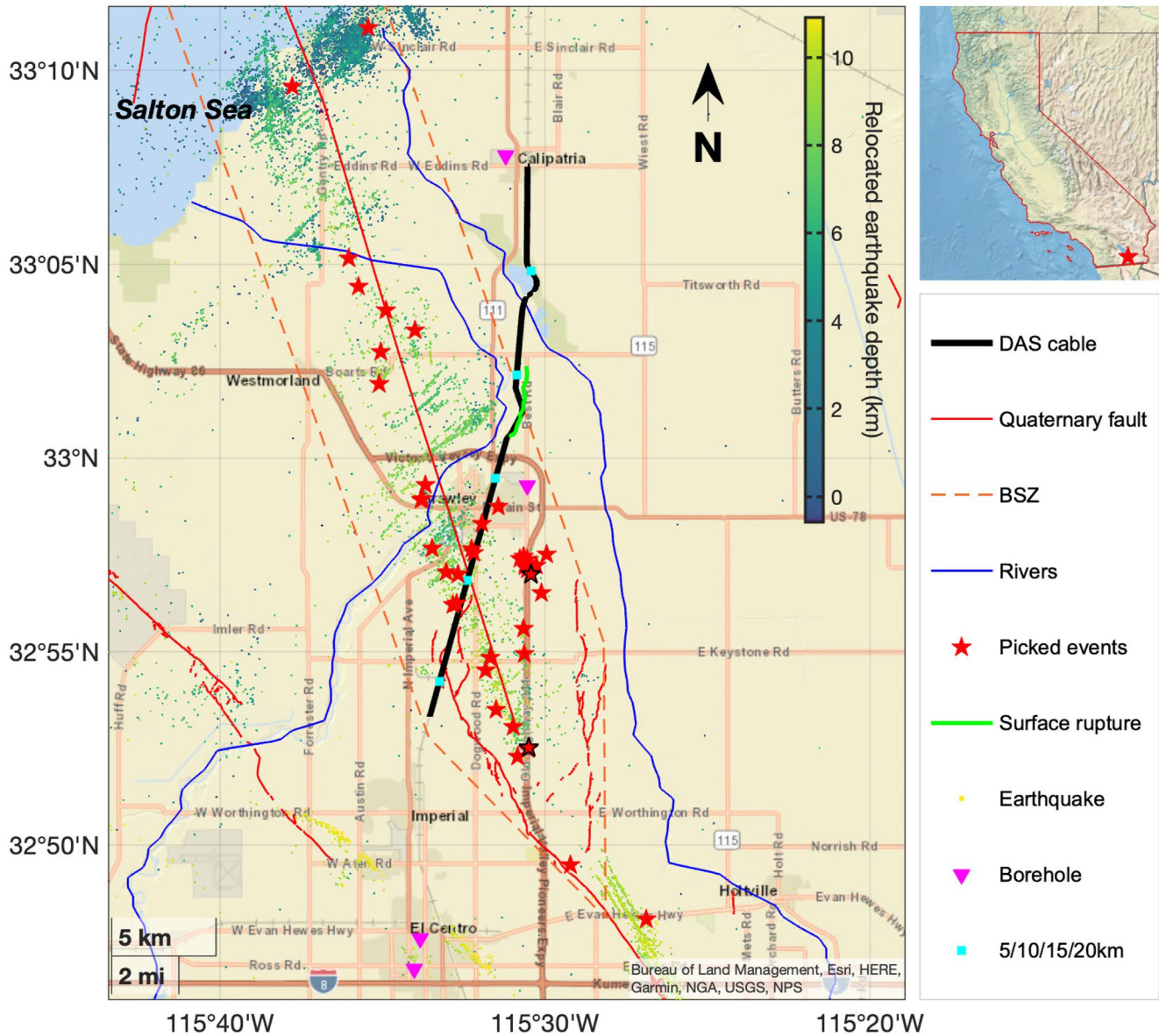


**Figure 1.** Site overview of the Imperial valley dark fiber experiment. Map of the Imperial Valley with DAS cable array (black line), Quaternary faults (red lines), Brawley seismic zone (BSZ, orange dash line polygon), rivers (Alamo River and New River, steelblue lines), USGS wells for downhole seismic velocity survey (magenta triangles), surface rupture (yellow line) due to the 2012 Brawley swarm, and historical earthquakes from 1981 to 2019 (blue-to-green colored dots). The colors of the earthquakes are coded by the relocated depths (Hauksson et al., 2012). The 40 red stars show the earthquake events picked during DAS observation; two events, highlighted with black edges, show the locations of the events displayed in the following study. The 5 cyan squares mark the cable length at the 5/10/15/20/25 km locations, with zero referring to the north end of the DAS array.

This model compares favorably with other ground-truth observations of near-surface structure acquired in the basin. We then conduct preliminary tests using local earthquake events observed in the DAS array for site effect evaluation and compare these measurements of ground motion with our high-resolution near-surface  $V_s$  model and  $V_s/30$  profile. Our results indicate that it is feasible to use such passive DAS surveys for near-surface structure characterization and site response estimation at large scale and high resolution, a combination useful for hazard microzonation.

## 2. Experiment and Data

Our experiment was carried out in the Imperial Valley with a fiber-optic telecommunication cable across the sedimentary basin, and it was designed to map and monitor geothermal resources at the basin scale using dark fiber

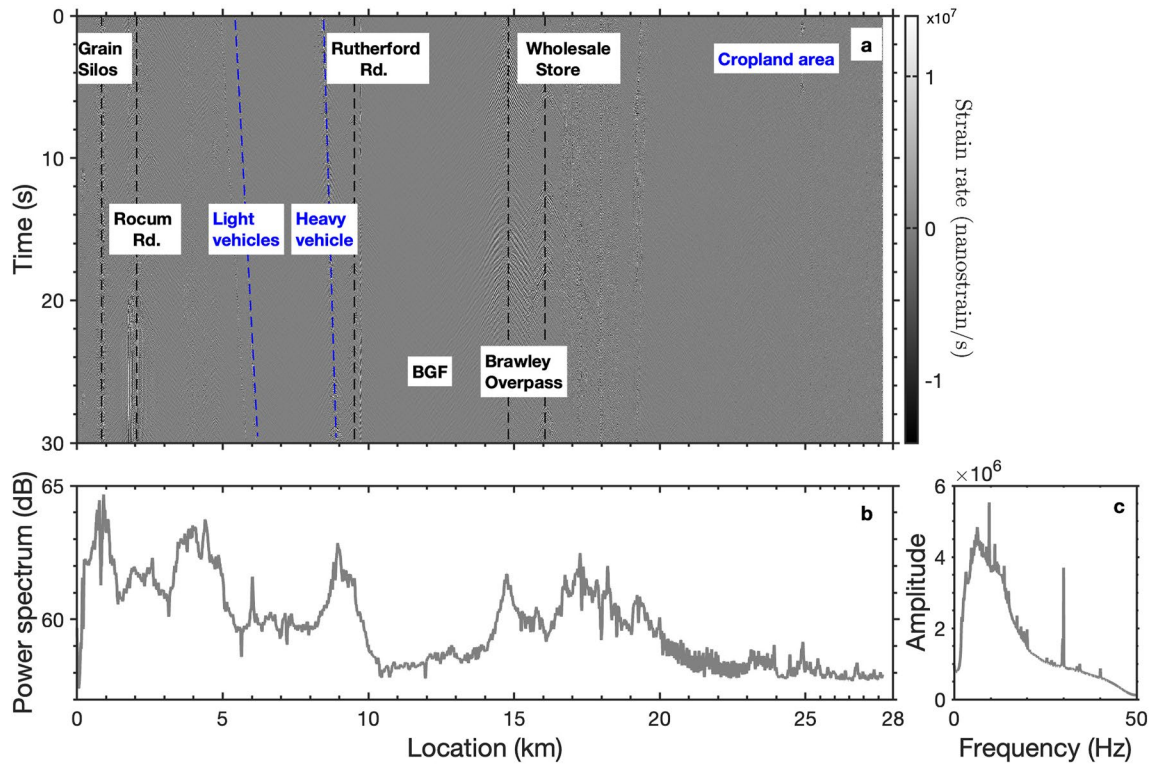


**Figure 2.** Observations of ambient noise on ~28 km DAS array. (a) 30-s ambient noise record of strain-rate (unit, nanostrain/s) with seismic signatures from moving vehicles and persistent localized sources, such as factories, crossing roads, Brawley Bypass. (b) The frequency-averaged power spectrum of ambient noise along the cable. (c) The spatially averaged amplitude of ambient noise along the cable.

and DAS (Ajo-Franklin et al., 2022; Cheng et al., 2023a). Taking into account the distributed sensing property of DAS, this data set also allows one to investigate the strengths of DAS for various purposes of seismic imaging at variable scales. The total cable length (~65 km) exceeded the distance that the Silixa iDAS v2 interrogator unit (IU) used in this experiment was capable of probing; we only utilized the first 28 km of fiber in the northern section of the cable (the black line in Figure 1) for DAS observations. The gauge length is set as 10 m, and the laser pulse rate is 2 kHz. The native strain-rate measurement is recorded with a 500 Hz sampling rate and a 4 m channel interval. The DAS channel locations along the fiber profile are calibrated by tap tests. An introduction to the experiment has recently been described in Ajo-Franklin et al. (2022), and our investigation of the potential of dark fiber DAS in combination with ambient noise interferometry for geothermal exploration is shown in Cheng et al. (2023a).

After acquisition tests, the DAS IU continuously recorded ambient noise data over the ~28 km cable length (total 6,912 channels) between 10 November 2020 and the spring of 2022, with some gaps due to instrumentation issues. This study, as part of the long-term DAS seismic monitoring project, only utilized the first 2-day data chunk to evaluate the feasibility of utilizing short duration DAS ambient noise data for high-resolution near-surface site effect estimation.

Due to dense spatial sampling of DAS, seismic signatures associated with various anthropogenic sources across the 28 km-long fiber can be easily identified from ambient noise records. For example, moving vehicles with various weights (blue dashed lines) and persistent localized sources (black dashed lines with nearly vertical moveout) are distinguished in Figure 2a. Complex human activities across the valley generate abundant energy between 1 and 20 Hz, which is a useful spectral band for typical near-surface characterization (Asten et al., 2022; Foti et al., 2018; Xia et al., 2009). However, the non-uniform distribution of anthropogenic sources, such as persistent localized sources with strong spatial consistency, might affect the signal retrieval during ambient noise interferometry (Cheng et al., 2023a); this challenge will be discussed in later sections.

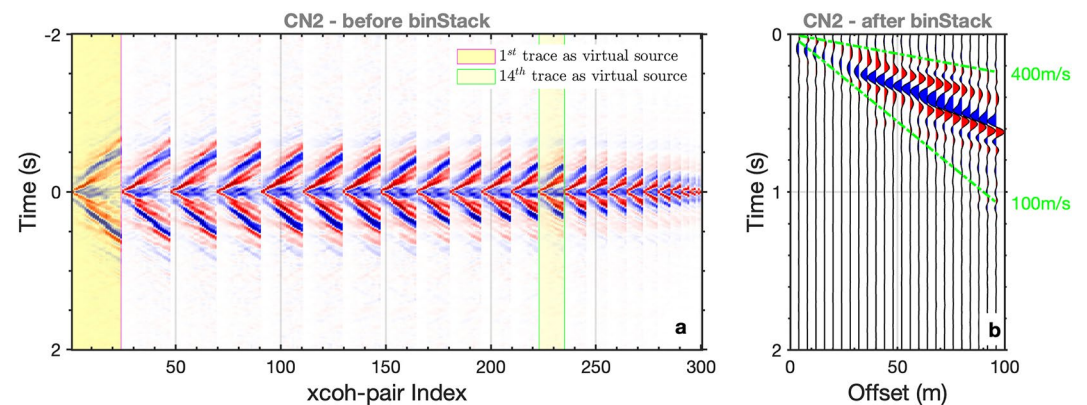


**Figure 3.** Empirical Green's function retrieval using ambient noise interferometry and bin stacking. (a) The EGF extracted from  $C_N^2$  inter-station cross-coherence pairs using ambient noise interferometry. The yellow boxes highlight the virtual-source gathers with the first trace and the 14th trace as the virtual sources, respectively. (b) The enhanced EGF after bin stacking with an offset bin of 4 m. Two green dashed lines indicate the reference velocity of 100 and 400 m/s.

### 3. Methods

#### 3.1. Ambient Noise Interferometry

Empirical Green's function (EGF) can be extracted from ambient noise records using ambient noise interferometry (Bensen et al., 2007; Shapiro & Campillo, 2004). Our data processing approach broadly follows the strategy introduced in Cheng et al. (2023a), and includes DAS ambient noise preprocessing, EGF extracting, and virtual-source gather (VSG) stacking. For more details regarding the DAS ambient noise data processing, we refer the reader to Cheng et al. (2023a).

In order to suppress effects of persistent localized noise sources as mentioned above, we apply a bin-offset stacking technique on all possible inter-station EGF pairs which are extracted using cross-coherence after 2-day phase-weighted stacking (PWS). See Figure S1 in Supporting Information S1 for the source and receiver configuration of all  $C_N^2$  inter-station interferometric pairs, where  $C_N^2 = 1 + 2 + \dots + n - 1$  and  $n$  denotes the channel number of each subarray. This technique has recently been used to improve EGF coherence at lower frequencies ( $< 3$  Hz) for this data set (Cheng et al., 2023a). The cross-coherence EGFs after temporal stacking (PWS) and spatial stacking (bin-offset stacking) can be used for subsequently dispersion imaging. The offset-sorted super gather or multiple virtual sources gather (VSG) in Figure 3b has been significantly improved compared to the conventional single virtual source gather as highlighted in Figure 3a (see Figure S2 in Supporting Information S1 for a side-by-side comparison). It is worth mentioning that the offset bin is set as 4 m, which is identical to the spatial interval of the raw DAS channels. Considering that the stacking process mitigates local lateral heterogeneity within each subarray, the lateral resolution of the raw subarray will be smeared. Therefore, this technique cannot be directly used for 2D seismic imaging, for example, full waveform inversion (Sager et al., 2018; W. Wang et al., 2017), adjoint tomography (K. Wang et al., 2021; Zhang et al., 2018) and wave-equation dispersion inversion (Li et al., 2017; H. Liu et al., 2022); while it would be appropriate for our dispersion curve inversion where 1D or layer model is assumed.

#### 3.2. Surface Wave Dispersion Measurements

After coherent signal retrieval using ambient noise interferometry, we utilized a MASW roll-along strategy (C. B. Park, 2005; Song et al., 1989) for our linear array surface wave dispersion imaging. We divide the entire DAS array into a series of shorter subarrays, whose length allows one to sample the expected wavelengths for near-surface  $V_s$  structure imaging. Compromising between the depth of investigation and the lateral resolution for near-surface characterization (Foti et al., 2018; Xia et al., 2006), a 100 m subarray was selected and rolled along the DAS cable without coverage subarray overlap. Across the 28-km telecommunication cable, this process generated a total of 273 short subarrays where the enhanced VSG was analyzed for surface wave dispersion measurement. Cheng et al. (2023a) utilized the same DAS data set to image the deeper geothermal reservoir by resampling the distributed strain-rate array into a series of longer subarrays (5 km) to extract the lower frequency surface waves.

The versatility of this data set demonstrates the potential of using DAS for multi-scale and multi-purpose seismic imaging.

According to Cheng et al. (2023b), passive-source surface wave dispersion analysis methods can be broadly grouped into non-interferometric methods (e.g., ReMi and PMASW) and interferometric methods (e.g., MAPS and SPAC). The former directly extract phase velocity dispersion spectra from ambient surface wave records (Louie, 2001; C. Park et al., 2004), while the latter calculate interferograms before dispersion estimation is attempted; in this case interferograms are either EGFs (e.g., Cheng et al., 2016) or SPAC coefficients (e.g., Asten, 2006; Chávez-García et al., 2006). To ensure the accuracy of dispersion measurements and estimate their uncertainties (Vantassel & Cox, 2021), for the first time, we tested three different techniques (MAPS, SPAC, and ReMi) in this study and evaluated their performance on DAS ambient noise dispersion imaging.

We follow Cheng et al. (2023b) to briefly introduce the data processing involved in the three dispersion measurement techniques. For MAPS, we apply the phase-weighted slant-stacking algorithm (Cheng et al., 2021) on the retrieved EGFs enhanced by bin-offset stacking, and measure the dispersion spectra  $E(f, v)$  using

$$E(f, v) = \omega(f, v) \left| \sum_{j=1}^N \exp(i2\pi f x_j / v) C_j(f) \right| \quad (1)$$

where,  $\omega(f, v)$  denotes the phase-weight for the slant-stacking enhancement, which is calculated by the instantaneous phase of the slant-stacking complex spectra (Equation 5 in Cheng et al. (2021));  $C_j$  denotes the enhanced EGF (the cross-coherence function) at offset  $x_j = (j - 1) * dx$  (note that,  $dx$  is the offset bin which is equal to the channel interval of DAS in this case);  $N$  denotes the channel number of the subarray;  $f$  and  $v$  denote the scanning frequency and velocity parameters, respectively.

For SPAC, we follow Chávez-García et al. (2006) to estimate the misfit between the SPAC coefficient  $\rho$  and the zero-order Bessel function of the first kind  $J_0$ ,

$$E(f, v) = \left( \sqrt{\sum_{j=1}^N |\rho(x_j, w) - J_0(x_j, k)|^2} \right)^{-1} \quad (2)$$

where,  $k = 2\pi f / v = w / v$ . Here, we use the inverse of the misfit to keep it consistent with other measurements. The SPAC coefficient ( $\rho(x_j, w)$ ) is represented by the real part of the whitened cross-correlation (i.e., cross-coherence) spectrum.

Instead of executing the dispersion measurement after EGF retrieval, ReMi directly applies rand (tau-p) transform on the noise data of each time segment, and stacks dispersion spectra of all segments to enhance the quality with

$$E(f, v) = \langle |E(f, p)| + |E(f, -p)| \rangle \\ = \left\langle \left| \sum_{j=1}^N \exp(i2\pi f p x_j) u(f, x_j) \right| + \left| \sum_{j=1}^N \exp(-i2\pi f p x_j) u(f, x_j) \right| \right\rangle \quad (3)$$

where,  $u(f, x_j)$  denotes the preprocessed ambient noise waveform at offset  $x_j$ ;  $p = 1/v$  is the slowness;  $\langle \dots \rangle$  denotes the ensemble stacking of all time segments, which is a classical processing step to mitigate incoherent or random noise in ambient noise interferometry. Note that non-interferometric methods (e.g., ReMi and PMASW) implement the ensemble stacking in the spectral domain for the dispersion estimation, while interferometric methods (e.g., MAPS and SPAC) implement the ensemble stacking in the temporal domain for the EGF enhancement.

Figure 4 shows three examples of the DAS-based passive surface wave dispersion measurements at location 9 km (upper panels), 18 km (middle panels), and 13 km (bottom panels) using MAPS (a1, a2, a2), SPAC (b1, b2, b3), and ReMi (c1, c2, c3), respectively. Clear and continuous fundamental modes have been obtained and picked from most dispersion measurements. Note that the non-interferometric methods usually estimate higher apparent velocities; we followed Louie (2001) and Pancha et al. (2008) to carefully pick dispersion curves along the lower boundary, rather than the peak, of the dispersion energy. According to Louie (2001), this lower boundary effectively selects for array colinear wave propagation while the peak may indicate arrivals illuminating the array broadside.

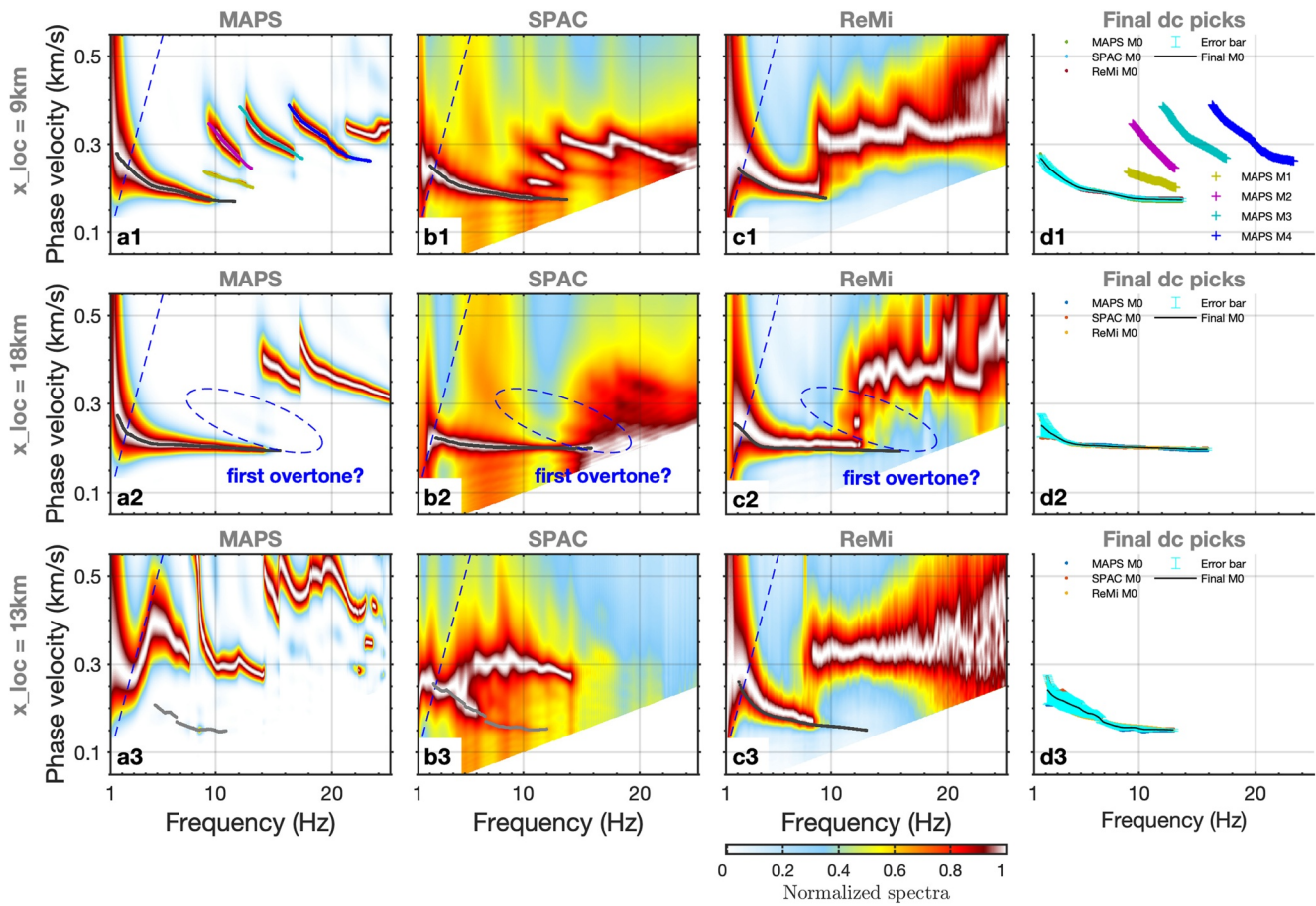


**Figure 4.** Surface wave dispersion measurements at location 9 km (upper panels), 18 km (middle panels), and 13 km (lower panels) using different techniques, including MAPS (a1, a2, and a3), SPAC (b1, b2, and b3), and ReMi (c1, c2, and c3), and the corresponding picked dispersion curves (d1, d2, and d3). The blue dashed lines indicate the potential maximum resolved wavelength inferred from the profile length. The gray dotted lines that overlay the dispersion spectra indicate the corresponding dispersion picks. The fundamental mode picks from different techniques closely match each other and are overlain with the cyan error bars. The black curves in the right panels show the final smoothed estimated fundamental modes. Note that the fundamental modes on a3 and b3 do exist but appear relatively weak compared with the stronger higher overtones, which are further highlighted by frequency normalized display.

Higher overtones have also been observed on most dispersion measurements, while different methods behave differently. The MAPS method provides the best performance and presents the higher overtones with sufficient resolution and a continuous energy trend. In contrast, the SPAC method shows lower sensitivity to the spectral peaks where higher overtones are located, and presents superposed modes rather than individual modes as shown on MAPS results. It is worth mentioning that a recently revisited technique, the frequency-Bessel transform (Forbriger, 2003; Hu et al., 2020; J. Wang et al., 2019; Xi et al., 2021), had also been tested and was also able to recover higher overtones as expected, but its stability is a bit unclear (in some cases, e.g., it would generate artifacts and mislead the identification of high overtones). Therefore, we did not include this method in our comparisons and further investigations are beyond the scope of this work.

Unfortunately, ReMi did not provide sufficient resolution to identify higher overtones due to the cross-talk between different modes, especially for these modes showing similar apparent velocities. However, ReMi appears to be more stable in terms of fundamental mode recovery, particularly for sites where noise sources are not uniformly distributed and only poor-quality EGFs are retrieved. For example, at the subarray centered around the 13 km location, both interferometric methods recover only weak discontinuous fundamental modes as well as distorted high overtones (Figures 4a3 and 4b3), while the non-interferometric method (ReMi) cleanly recovers the fundamental mode (Figure 4c3), particularly at low frequencies. As described above, interferometric methods only employ single-time dispersion measurement on the stacked VSG while non-interferometric methods average dispersion measurements of all individual time segments. Compared to the single-time dispersion measurement

for interferometric methods, the ensemble stacking provides non-interferometric methods the potential advantage to enhance the dispersion energy trend of the fundamental mode, because the lower boundaries are usually fixed although the apparent phase velocities are higher than true velocities. In this context, it could be helpful to employ non-interferometric measurements as references for fundamental-mode dispersion curve picking, particularly for cases where interferometric methods do not perform well.

With various independent fundamental-mode dispersion measurements observed at the same site, we have the opportunity to calculate the data error or uncertainties of the picked dispersion curves (Vantassel & Cox, 2021). We first extrapolated and combined three dispersion curves picks into a uniform maximum and minimum frequency range, then predicted a smoothed dispersion curve (the black solid line in d1 and d2) from the combined picks using the Gaussian kernel regression (Henderson & Parmeter, 2015). For each frequency, we can also estimate the root-mean-square (RMS) error (the cyan error bar in d1 and d2) between three fundamental-mode picks. Figures 4d1–4d3 demonstrate the high consistency of the picked fundamental modes between various dispersion measurements with picks from one method closely overlaying with picks from others. This exercise also increases our confidence in the accuracy and stability of our DAS dispersion measurements. We should note that the uncertainties captured are a combination of data noise and methodological biases in the different dispersion curve extraction algorithms and do not represent a true prior data covariance.

To avoid potential mode misidentification, we only pick higher overtones from MAPS measurements at sites where similar mode patterns can also be observed on SPAC or ReMi measurements despite their lower resolution. For example, we did not pick higher overtones in Figure 4a2 although clear higher overtones are visible at frequencies >15 Hz; because we can also detect weak and smeared dispersion energy with higher velocities around 300 m/s at frequencies <10 Hz on the SPAC measurement (highlighted with an ellipse in Figure 4b2) which is likely the first-order higher overtone. The cause of the disappearance of the higher overtone energy on MAPS measurement at location 18 km could be that the specified higher overtone is less horizontally polarized compared to the fundamental mode in the specified site. Spectral normalization along the frequency axis also decreases the weights of the higher overtones at frequencies <15 Hz. The phenomenon of jumps across more than one mode has also been observed by others (O'Neill & Matsuoka, 2005; Yan et al., 2022). For accurate dispersion curve picking, we limited the target zone and removed the energy beyond the maximum effective wavenumber range defined by  $k_{\max} = 1/dx$  ( $dx$ , spatial interval 4 m); we also paid special attention to picks at lower frequencies with wavenumbers below the minimum effective wavenumber  $k_{\min} = 1/L$  ( $L$ , array length 100 m) as indicated by the blue dashed lines. For higher overtones picks, we determined the picking error with the velocity interval between the boundaries of the 90% energy peak and the peak itself from each MAPS measurement.

### 3.3. Quality Control of DAS Dispersion Measurements

Unfortunately, not all dispersion measurements are acceptable for confident dispersion curve picking and inversion. In fact, around 15% of the dispersion measurements show a noisy spectral response with discontinuous energy trends regardless of the use of interferometric or non-interferometric methods. For these subarrays, it is challenging to pick continuous dispersion curves, particularly for the higher-frequency range from 5 to 20 Hz in which urban anthropogenic noise dominates the response. However, these higher-frequency Rayleigh waves are required to provide sensitivity at shallow depths for near-surface structure imaging.

We find that most of the poor dispersion measurements are observed at sites where persistent noise sources exist. Figure 5a displays the retrieved EGF before bin stacking for the subarray located near 15 km where the Brawley overpass crosses. If we focus on the VSG with the first trace as the virtual source (highlighted with the pink box in Figure 5a), we will find that the VSG is significantly different from the one shown in Figure 3a, with the retrieved surface waves presenting linear move-outs; in contrast, the VSG appears contaminated by a “left-going” wave train which actually originates from a persistent noise source located at the right end of the subarray. We observe that these “left-going” wave trains do not change as the virtual source moves. Note that when the virtual source is located on the right side of the persistent noise source, spurious arrivals shift to the negative time lag (highlighted with the green box in Figure 5a).

Although these spurious arrivals appear to have good signal-to-noise ratios (SNR) and high spatial coherency, they are non-physical (not part of a true Green's function) and are only related to the persistent noise source. Recent studies have attempted to utilize these spurious events for structural seismic imaging (Yang et al., 2022b).



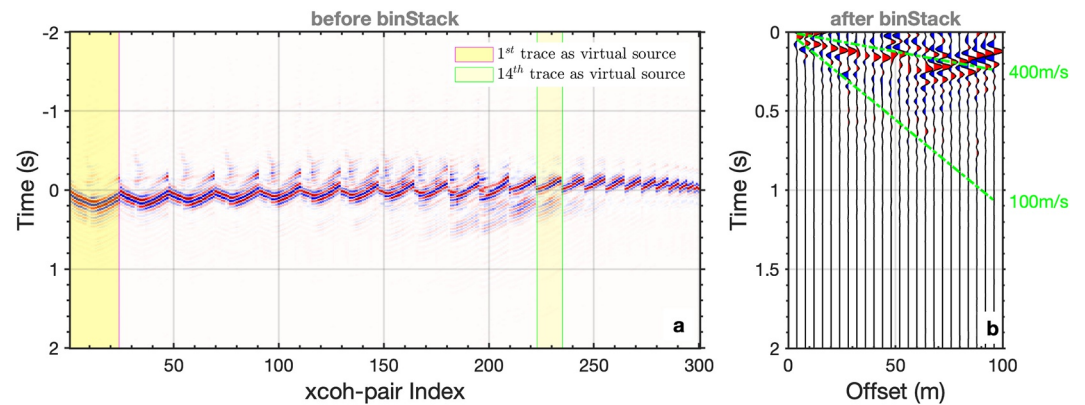


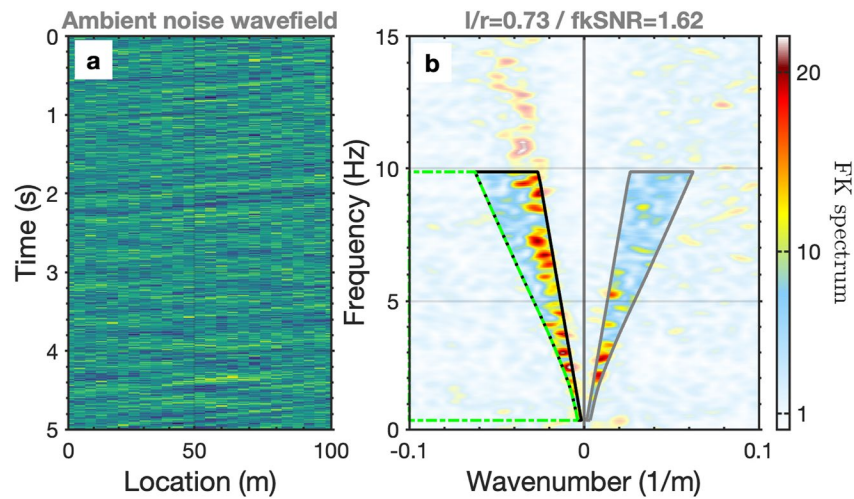
**Figure 5.** EGF retrieval as same as Figure 3 but with the existence of persistent noise sources around 15 km.

However, Cheng et al. (2023a) also indicates that the interpreter should check whether they are structure-related or source-related. In this study, we focus on strategies to attenuate these persistent noise sources and improve conventional ambient noise imaging. Assuming that we are using traditional two-station methods, for example, the frequency–time analysis (FTAN) method (Bensen et al., 2007; F.-C. Lin et al., 2008; Nayak et al., 2021), rather than the array-based dispersion imaging techniques mentioned above, these spurious arrivals would be misinterpreted as reasonable and high SNR arrivals and lead to highly inaccurate velocity estimates. It indicates that these array-based techniques, which are frequently used in near-surface seismology, could also be a promising alternative in tectonic seismology, particularly under the background of the rapid development of the dense array and DAS array observation techniques.

After bin stacking, spurious arrivals have been partly attenuated (Figure 5b) but still seriously obscure the target surface waves. This indicates that spatial averaging using bin stacking cannot completely eliminate persistent noise sources effects, at least for high-frequency ( $>5$  Hz) ambient noise. Because these persistent noise sources are spatially persistent and temporally frequent, they break the assumptions of randomly distributed noise sources that underlying most of the ambient noise interferometry theory. Traditional denoising techniques that aim to improve temporal coherency, for example, PWS (Schimmel et al., 2011) and the SNR selective stacking technique (Xie et al., 2020), cannot attenuate them; to improve surface wave retrieval, we must consider array-based techniques to enhance the spatial coherency of the retrieved surface waves (Cheng et al., 2018; Y. Liu et al., 2021). Several studies have been carried out to attenuate noise sources effects by using selective stacking strategy (Pang et al., 2019). If we can selectively stack time segments in which coherent noise sources dominate or dispersion spectra show high quality, we will be able to automatically enhance EGF retrieval or dispersion measurement. The challenge is to construct a criterion to evaluate the SNR of dispersion spectra.

In this study, we adapt the selective stacking technique developed by Cheng et al. (2018) and define a “SNR” concept by calculating the energy ratio between a target velocity zone (signal spectra window) and a background velocity zone (noise spectra window) in the frequency-wavenumber ( $f-k$ ) domain (Figure 6). The target velocity zone (the black polygon in Figure 6b) is outlined by a rough range of the prior picked fundamental-mode dispersion curves from a neighboring site; then the left lower-velocity zone beyond the target zone is simply defined as the background noise zone (the green polygon in Figure 6b). Note that we do not include higher overtones into the signal spectra window to avoid confusing them with the higher velocity artifacts caused by off-line sources; we define the noise spectra window with the lower-velocity zone, which mainly represents the background  $fk$  spectra noise (or the geometry response in the  $f-v$  domain) and is usually affected by the noise source environment. We note that the window domain should be considered either a velocity prior or an inferred constraint extrapolated from nearby locations.

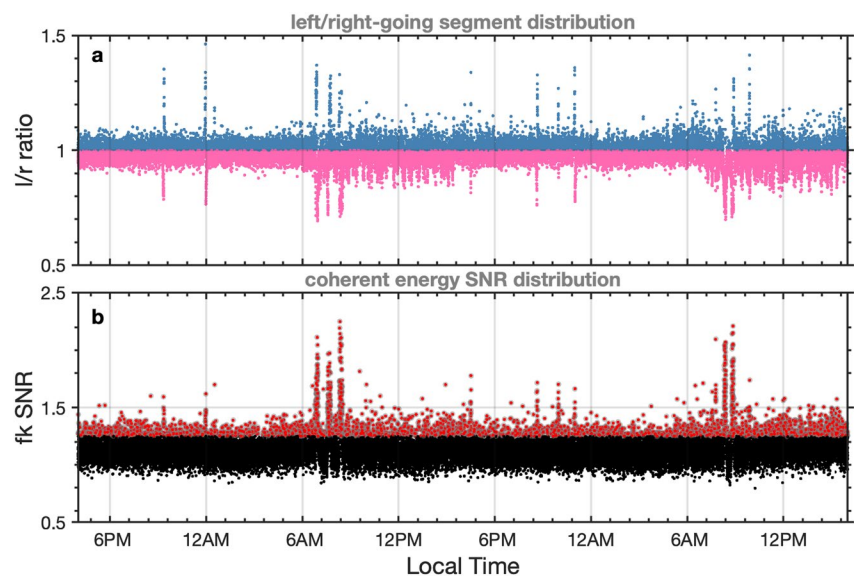
For simplicity, we calculate the  $f-k$  spectra for each time segment using the ambient noise wavefield (Figure 6a) rather than the interferogram wavefield. Taking into account the bidirectional characterization of ambient noise wavefield, we follow Cheng et al. (2018) to choose the wavefield with the dominant propagation direction to enhance the coherent signal. After transforming the ambient noise wavefield into the  $f-k$  domain, we first calculate the ratio of the target signal wavefield energy between the left-going wavefield (the black polygon in



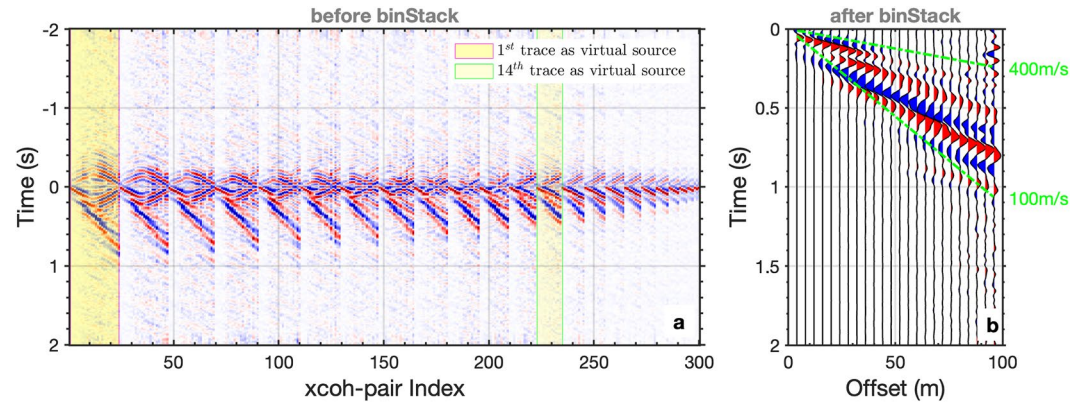
**Figure 6.** SNR estimation of the predominant coherent energy of DAS ambient noise segment for subarray around 15 km. (a) and (b) display the DAS ambient noise segment in the time domain and in the frequency-wavenumber domain, respectively. Two symmetric polygons represent the coherent energy zones of the interested left-going and right-going wavefield outlined with black and gray solid lines, respectively. The green polygon indicates the background noise zone used for the fkSNR estimation. The title of b shows the measured energy ratio ( $l/r$ ) between left- and right-going wavefield and the SNR of coherent energy (fkSNR).

Figure 6b) and the right-going wavefield (the gray polygon in Figure 6b), called the “ $l/r$ ” ratio. Then, we estimate the SNR of the coherent energy based on the  $f - k$  panel on the dominated propagation side. In this case, the dominant side is the left side  $f - k$  panel on Figure 6b, with  $l/r = 0.73 < 1$  indicating a strong left-going wavefield as shown by the left-going wave trains on Figure 6a. We call the defined “SNR” parameter fkSNR.

Figure 7 shows an example of a 2-day time distribution of the  $l/r$  ratio and fkSNR at a subarray location around 15 km. The symmetric  $l/r$  distribution around 1 represents the bidirectional traffic flow with spikes indicating traffic peaks, for example, the morning rush hour that occurs between 7 and 9 a.m. local time. The high correlation between the traffic peaks and the fkSNR peaks probably indicates that dense traffic noise sources contribute to coherent energy recovery, and hints that a promising approach might be able to shorten observation duration for



**Figure 7.** Time distribution of  $l/r$  (a) and fkSNR for subarray around 15 km (b). The pink and blue dots in a indicate the time segments dominated by the left- and right-going wavefield, respectively. The red dots in b indicate the selected time segments with fkSNR above the defined threshold (1.25).



**Figure 8.** EGF retrieval after persistent noise source attenuation using the proposed fkSNR selective stacking. (a) Shows the  $C_N^2$  cross-coherence pairs after selective stacking with segments above the defined fkSNR threshold; (b) shows the corresponding enhanced EGF gather after binstack of all  $C_N^2$  pairs in (a).

passive seismic imaging to coincide with the busy traffic period. To reject time segments with poor coherent energy, we simply set a hard threshold for fkSNR; in this study, trials indicated fkSNR above 1.25 (highlighted with red scatters) were sufficient for passive surface wave imaging under the urban ambient noise environment in the Imperial Valley. Compared with the full stacking result (Figure 5a), the retrieved EGF after selective stacking shows enhanced Rayleigh waves as well as attenuated spurious arrivals (Figure 8a). Note that it is also possible to further eliminate these spurious arrivals with a higher threshold but with the cost of fewer stacked records, which might degrade the retrieved EGFs. We focus on ensuring the quality of the retrieved EGFs, since leaky spurious arrivals can also be further attenuated by spatial averaging and bin stacking, as shown in Figure 8b.

With enhanced EGFs (Figure 8b), the interferometric methods (MAPS and SPAC) can successfully extend the dispersion measurement band from 5 Hz (Figures 9a1 and 9b1) to over 10 Hz (Figures 9a2 and 9b2) and improve the lower frequency band (<5 Hz) with more continuous dispersion energy trends; these attributes are vital for subsequent dispersion curve picking. Higher overtones were also retrieved from enhanced dispersion measurements (Figures 9a2 and 9b2). As for the non-interferometric method (ReMi), we selectively stack dispersion measurements of time segments with high fkSNR. A clear and continuous fundamental mode has been revealed on the enhanced ReMi measurement (Figure 9c2). Unfortunately, as mentioned previously, it remains challenging to enhance the higher overtones for non-interferometric measurements because they are easily polluted by artifacts from off-line sources.

#### 4. Results

To extract 1D  $V_s$  profiles for each subarray, we jointly invert the multiple-mode dispersion curves by following Cheng et al. (2023a). In this study, we initialize the earth model (Table 1) based on an averaged velocity model from USGS borehole surveys (Porcella, 1984). Figure 10 shows two examples of DAS-based surface wave inversion with multiple modes and the fundamental mode, respectively. Acceptable misfits can be obtained for both examples. In addition, the more convergent inversion models in Figure 10b compared to that in Figure 10d indicate the advantage of higher overtones to constrain a deeper structure, in contrast to using the fundamental mode alone (Xia et al., 2003). Finally, the best-fit 1D  $V_s$  profiles for all subarrays are aligned along the DAS cable to construct a pseudo-2D  $V_s$  structure.

The high-resolution  $V_s$  model (Figure 11a), derived from the DAS array, shows generally uniform sediment properties below 30 m depth overlain with several zones of softer materials throughout the 28 km cable. Around 7 km where the DAS cable crosses the Alamo River and is deployed along the side of Ramer Lake, a low-velocity surface unit is visible on the inverted  $V_s$  structure and is interpreted as a soft fluvial and lacustrine clay and sand deposit. The soft zone between 10 and 15 km might be associated with unconsolidated surface materials along the southern section of the Brawley Seismic Zone, where surface rupture (the green line in Figure 1) had been observed in the 2012 Brawley Swarm. An alternative hypothesis could link lower velocities to recent fluvial sediments deposited by the New River (the blue line on the left side of Figure 1). The soft zone in the south might be caused by tilled crop land with high soil moisture due to historical agriculture and irrigation. The slightly slower sediments to the north end are likely linked to deepening lacustrine sediments as we approach the Salton Sea. Historical soil samples collected in nearby boreholes below 30 m show sandy silt with lenses of

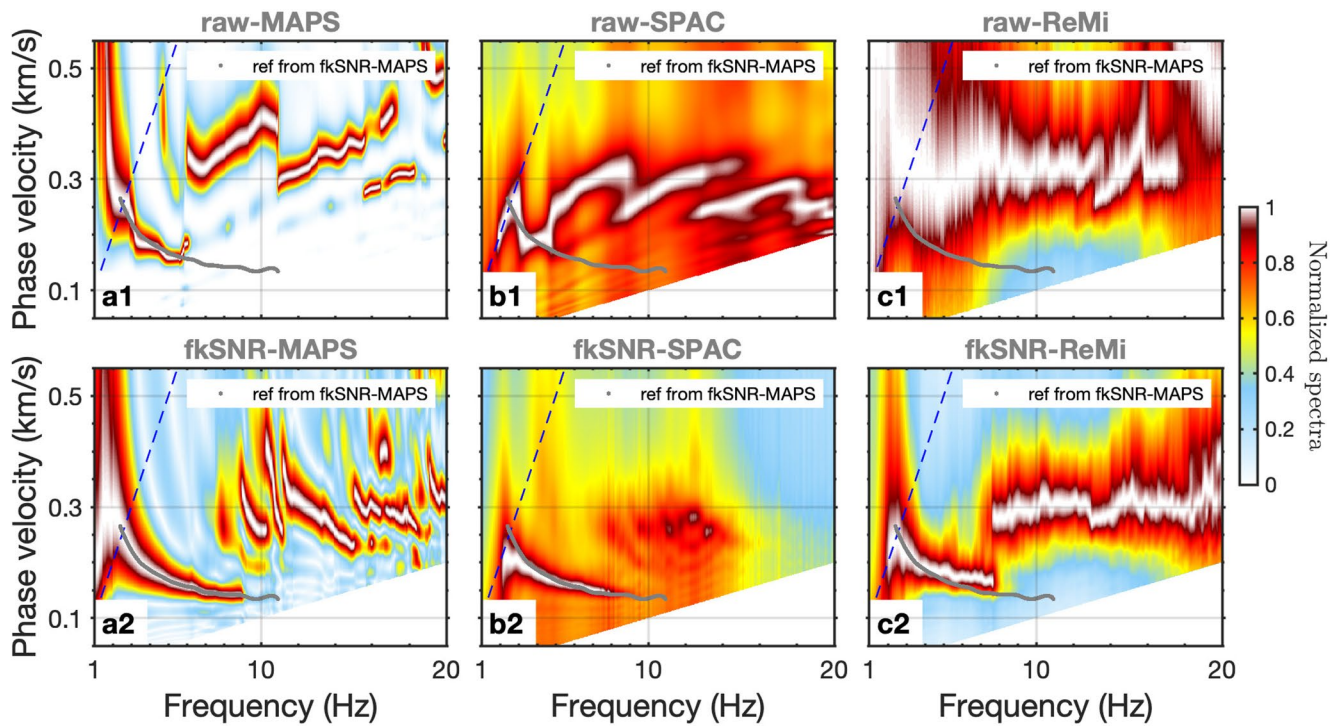


**Figure 9.** Performance of fkSNR selective stacking on improving surface wave dispersion measurements. The upper panels show the dispersion spectra before data selection using different techniques, including MAPS (a1), SPAC (b1), and ReMi (c1). The lower panels show the corresponding dispersion spectra after data selection using different techniques, including MAPS (a2), SPAC (b2), and ReMi (c2). The gray dotted lines indicate the reference dispersion curves picked from the enhanced MAPS result (a2).

soft grayish-brown clay in Calipatria transitioning to fine to very fine, well-sorted brown, silty sand in Brawley (Porcella, 1984).

To further study lateral variations across the DAS profile, we explored the ambient noise autocorrelation. This technique has been successfully applied to image the subsurface structure on both Earth and Mars (R. W. Clayton, 2020; Deng & Levander, 2020), and has recently been used with offshore DAS data to image the marine sediment structure (Spica et al., 2020a). Before applying the autocorrelation algorithm (zero offset cross-correlation) to the densely sampled DAS array, we adapted our previously utilized data preprocessing workflow by replacing the spectral whitening algorithm with a spectral despiking algorithm using a histogram approach (Solomon et al., 2001) to attenuate narrow-band artifacts in the DAS autocorrelation functions (see Figure S3 in Supporting Information S1 for details on the performance of the spectral despiking algorithm). The resulting autocorrelation profile (Figure 11b) indicates a distinct lateral variation across the 28 km-long cable with high spatial resolution (4–10 m). Taking into account the dominant surface waves observed from the surface DAS array, it might be inappropriate to interpret the autocorrelation horizons as specular reflections as indicated in previous studies (Oren & Nowack, 2016; Spica et al., 2020a). An alternative hypothesis might interpret that portion of the zero-offset EGF as representing localized surface wave scattering rather than specular S/S reflections. In both cases, we would predict lateral moveout variations of the zero-offset EGF coincident with lateral discontinuities in subsurface velocity structure, which is the response that we observe. We note that the lateral variations of the autocorrelation profile match well with variations in the depth of the  $V_s = 200$  m/s isocontour (highlighted with the red line) where the bottom of the soft and unconsolidated overlay likely generates an impedance contrast, and the consistency in some degree indicates the accuracy of both observations.

To further evaluate the accuracy of our DAS  $V_s$  profile, we compare the inverted  $V_s$  model with velocity models determined by USGS downhole

**Table 1**  
Prior Boundaries of Uniform Probability Distributions Used for Each Parameter of the Depth Model

Layer number	Thickness (m)	$V_p$ (m/s)	$V_s$ (m/s)	Density ( $\text{g/cm}^3$ )
1	2–8	215–650	60–250	2.0
2	4–12	335–1,000	85–335	2.0
3	5–15	400–1,200	95–380	2.0
4	12–35	500–1,500	125–500	2.0
5	5–15	600–1,800	135–535	2.0
Half-space	10–30	760–2,300	175–700	2.0

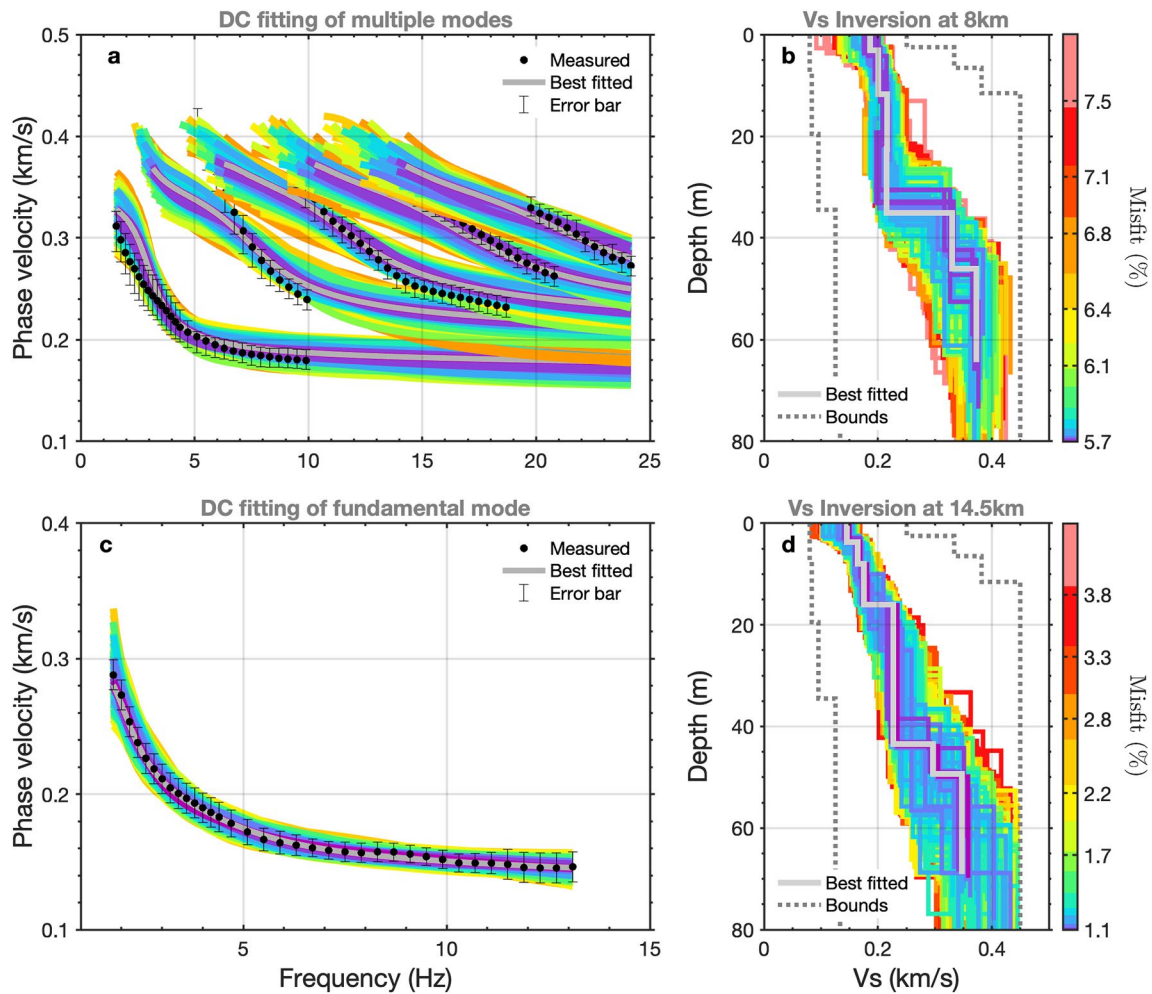


**Figure 10.** Surface wave inversion using multiple-mode (the upper panels) and single mode (the lower panels) dispersion curves. (a) Shows the measured (the black dotted curves) and the best 400 forwarded (the colored curves) multiple-mode dispersion curves; the gray curves show the dispersion curve forwarded from the best-fit model. (b) Presents the corresponding best 400  $V_s$  models at 8 km location; the gray curve indicates the best-fit model; the dashed lines indicate the upper and bottom velocity boundaries. (c) and (d) show the same example at 14.5 km location with single-mode dispersion curve inversion. Colors in each row are coded by misfits as shown on the right-side color map.

velocity surveys (Porcella, 1984; Warrick, 1974). We selected the four closest boreholes distributed from the north to the south of the cable as reference and compared the reference 1D velocity models (the colored lines in Figures 12a–12c) with our inverted models from DAS (the black lines in Figures 12a–12c). Overall, our inverted models match well with the reference models from borehole surveys in terms of both absolute values and recovered  $V_s$  gradients. Due to the layered parameterization, not all local interfaces are identical, but the average values are quite comparable, particularly given the spatial offsets with the ground-truth boreholes; this similarity bolsters our confidence in the inversion results.

Based on the inverted  $V_s$  model, a high-resolution  $V_{s30}$  profile (the magenta curve in Figure 12d) along the 28 km DAS cable is estimated in accordance with the following expression

$$V_{s30} = \frac{30}{\sum(h_i/v_i)} \quad (4)$$

where  $h_i$  and  $v_i$  denote the thickness and shear-wave velocity of the  $i$ th formation or layer existing in the top 30 m. To avoid the potential uncertainties related to our inversion strategy, we compare this estimate to an alternative technique to calculate  $V_{s30}$  without inversion. Past studies have shown that Rayleigh-wave phase velocity at a wavelength of 36 m,  $v_{r36}$ , is highly correlated with  $V_{s30}$  (Brown et al., 2000; S. Lin et al., 2021; H.-Y. Wang & Wang, 2015). The most practical equation is

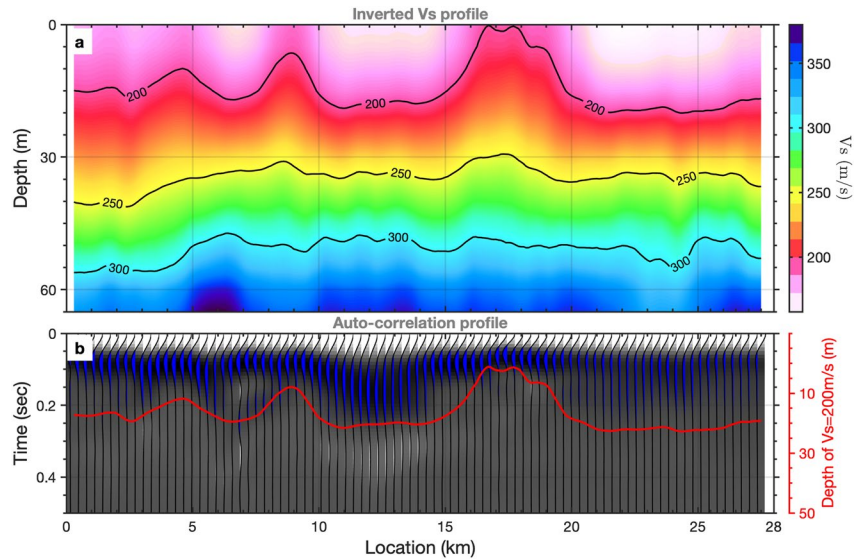


**Figure 11.** Ambient noise imaging of near-surface structure of the Imperial valley. (a) The inverted  $V_s$  model from DAS ambient noise data. The black lines depict the velocity contour lines of 200, 250, and 300 m/s. (b) The extracted autocorrelation profile along the entire profile. For a better display of the autocorrelation profile, the interval-distance has been resampled to 20 m; bandpass filter (1–10 Hz) is applied. The red line shows the contour line of 200 m/s in a, which likely indicates the depth of the surface soft clay layer of the Imperial Valley.

$$V_{s,30} = 1.076v_{r,36} \quad (5)$$

with a 95% confidence interval of approximately  $\pm 10\%$  (Brown et al., 2000). Therefore, a secondary  $V_{s,30}$  profile (the green curve in Figure 12d) is calculated for each site based on the picked fundamental-mode Rayleigh-wave dispersion curves. As expected, it is quite similar to the  $V_{s,30}$  profile estimated from surface wave inversion. The RMS error between the two  $V_{s,30}$  profiles is  $\sim 3\%$ .

This is one of the first estimates of fine-scale  $V_{s,30}$  profiles at basin scales above 20 km with 100 m spatial resolution. Note that this spatial resolution ( $\delta$ ) can be further refined to tens of meters with the appropriate subarray length ( $L$ ) and the moving step ( $D$ , the spatial interval between two neighboring subarrays; in this case  $D = L$  since there is no overlap between the subarrays). Generally, the finest spatial resolution could be the moving step (i.e.,  $\delta \geq D$ ), and the coarsest spatial resolution should be the subarray length due to the 1D assumption (i.e.,  $\delta \leq L$ ). In practice, reproducing this work with conventional point geotechnical investigation methods would be prohibitively expensive.

Likewise, the remote sensing derived  $V_{s,30}$  model based on local geology and terrain slope cannot capture the expected variations along our 28 km profile (McPhillips et al., 2020; Wills et al., 2015) either. Figure 12d shows the dramatic difference between our high-resolution  $V_{s,30}$  profile (colored lines) and the low-resolution model (gray line) interpolated from Thompson et al. (2014) based on geological priors and topography. Following the USGS borehole survey (Porcella, 1984), we believe that the model of Thompson et al. (2014) generally overestimates the  $V_{s,30}$  across the basin area with some local areas showing 100 m/s higher than the average  $V_{s,30}$  ( $\sim 200$  m/s). However, this biased  $V_{s,30}$  model from Thompson et al. (2014) has been widely used by the seismology community; for example, the Unified Community Velocity Model (UCVM) software framework has utilized this model as the geotechnical layer (GTL) (Ely et al., 2010; Maechling et al., 2019). We know that the near-surface soil layers of sedimentary basins play a critical role in modifying the amplitude, frequency, and duration of earthquake ground shaking. Our near-surface velocity model has been verified at available ground truth locations and proves to be accurate at high resolution (tens to hundreds meters) at the basin scale. These results suggest that the model is a promising alternative for fine-scale ground motion estimation.

## 5. Discussion

The dense spatial sampling and spectral bandwidth of DAS allow for observations of local earthquakes and teleseismic events (Ajo-Franklin et al., 2022; Lindsey et al., 2017; H. F. Wang et al., 2018; Yu et al., 2019).

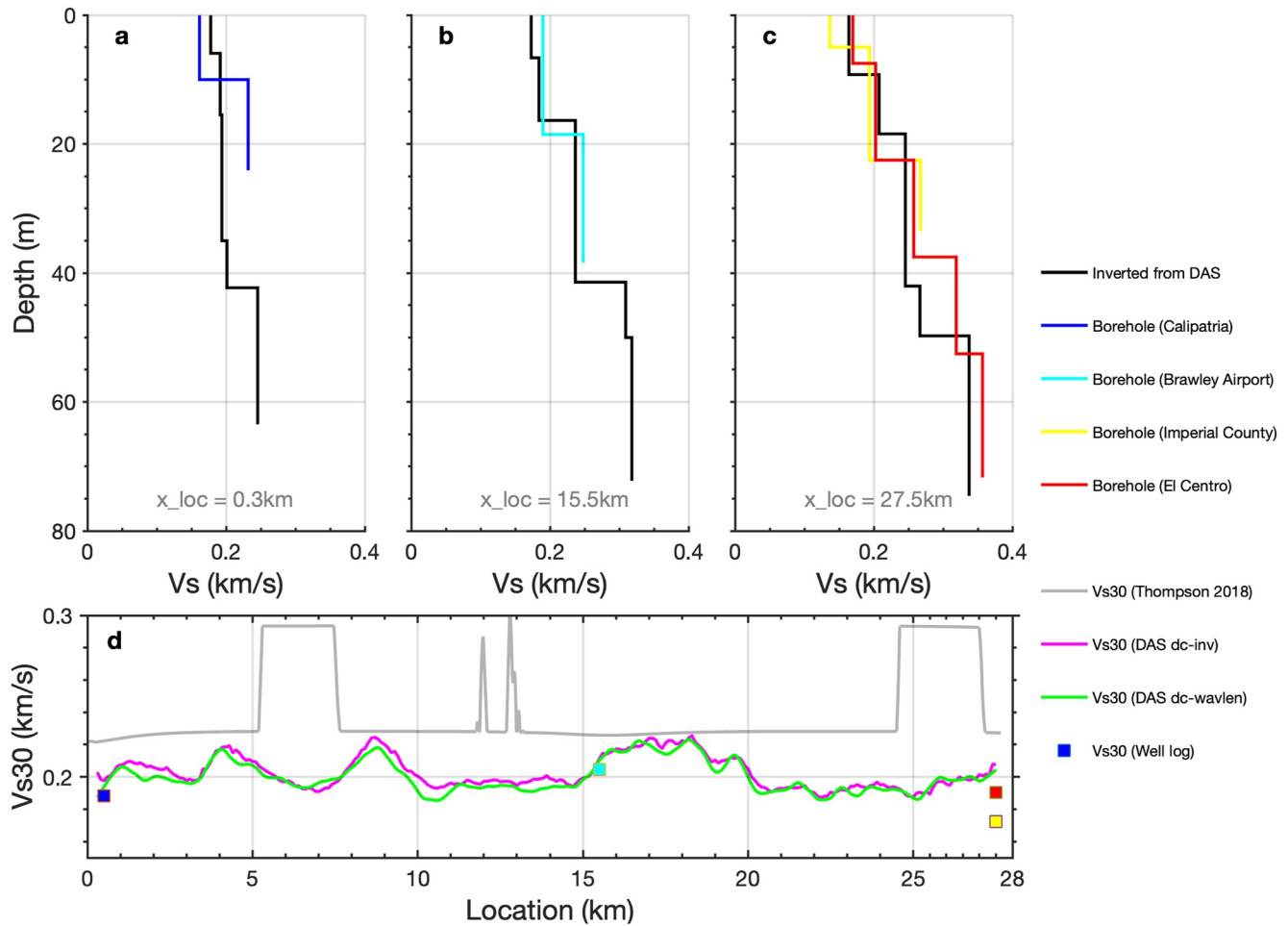


**Figure 12.** Accuracy of the estimated velocity model. (a and c) Comparisons between the inverted 1D  $V_s$  model and the nearby downhole  $V_s$  survey measurements (Porcella, 1984). (d) Comparison between the geology-based  $V_{s30}$  profile (the gray line) interpolated from Thompson (2018) and the seismic-based  $V_{s30}$  profiles (the colored lines) measured from DAS along the cable. The magenta line shows the  $V_{s30}$  estimated using the inverted  $V_s$  models (Equation 4); the green line shows the  $V_{s30}$  converted from the picked dispersion curves (Equation 5); the square dots show the  $V_{s30}$  converted from the nearby downhole  $V_s$  logs. Note that the bias of  $V_{s30}$  between the DAS and the downhole survey at the south end could be caused by the lateral heterogeneities of the surface structure considering that the two wells (red and yellow squares) are more than 12 km away from the south end of the DAS array (see the borehole locations in Figure 1).

Thousands of events have been recorded on the Imperial Valley DAS cable since November 2020. They provide a secondary data set, beyond surface waves, for potential site response and ground motion analysis. In this study, we conduct preliminary tests using 40 high-quality selected events from the Southern California Earthquake Data Center (SCEDC) catalog (see Table S1 in Supporting Information S1 for details of the catalog).

Like surface wave analysis discussed previously, the observed earthquake events, particularly the small local earthquake events, are usually contaminated by persistent noise sources. To denoise events, we first follow the protocol of Yang et al. (2022a) to convert the DAS strain rate wavefield to particle motions using the Cartesian cornea framework of the fast discrete curvelet transform (Atterholt et al., 2022). A recent study (Chen, 2023) also indicates that DAS raw strain rate data can be used directly to estimate spectral source parameters without conversion to particle velocities. We next applied a linear-moveout (LMO) corrected FK filter to further remove persistent noises distributed across our 28 km cable. To avoid potential interference with event recovery, we used LMO correction to flatten the S wave direct arrivals before FK filtering, and unflatten the records after removing the low-velocity (<1 km/s) noise components. Here, we focus on S waves because of their higher SNR on the horizontal DAS array compared to near-vertically incident P waves. To reduce computational burden and increase data quality, we resampled the DAS array in a 20-m spatial interval with spatial median stacking (5 channel window) for this analysis. Figure 13 shows two typical examples of DAS earthquakes denoising. The denoising workflow results in cleaner enhanced S arrivals (Figures 13b and 13d) without the footprint of noise sources

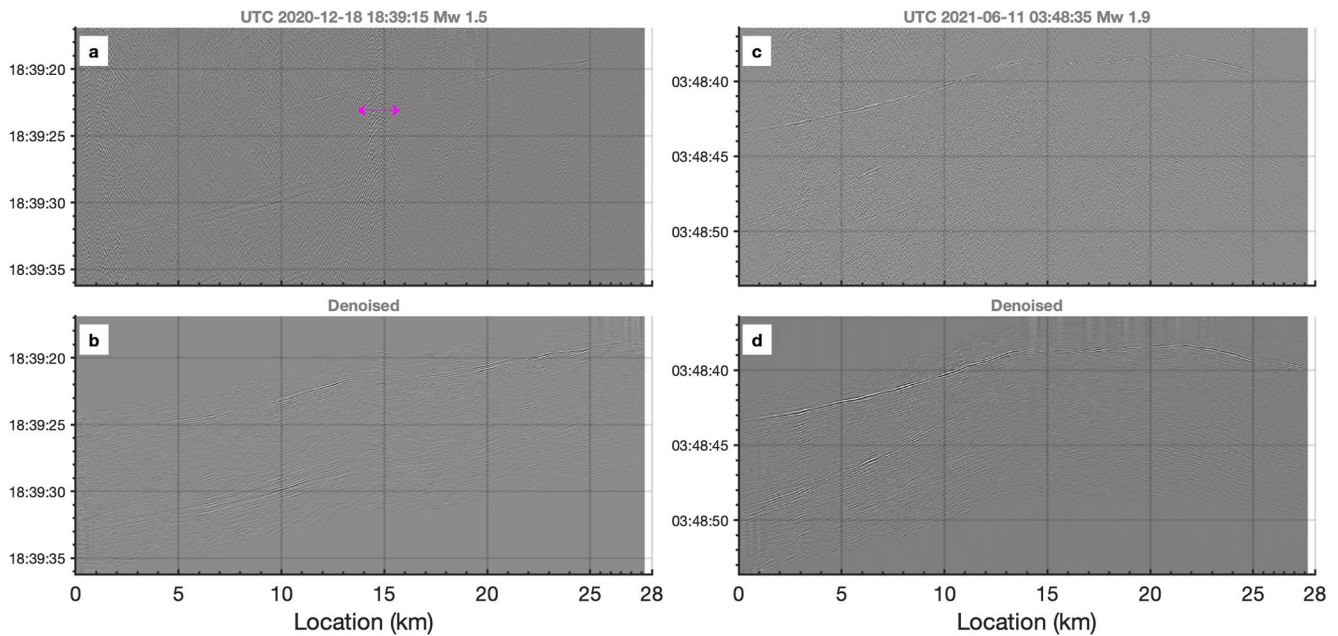


**Figure 13.** Examples of the observed earthquake events before (a and c) and after (b and d) denoising. The red curves show the estimated  $V_s30$  profile using the inverted  $V_s$  models. The magenta double arrow indicates the locations of the persistent noise sources. Both events have been highlighted in Figure 1 as red stars with the black edge.

along the array. Note that the denoised arrivals around 15 km (Figure 13b) show relatively lower SNR compared with arrivals in other locations, although signatures associated with persistent noise sources (highlighted with the double arrow on Figure 13a) have been significantly attenuated.

We followed Yang et al. (2022a) to estimate site effect magnitudes by using a spectral decomposition method (Andrews, 1986; Shearer et al., 2006). We picked S wave arrivals for all 40 events, and cut the denoised wavefield to record windows of 2 s before and 10 s after the picked arrivals. Next, we calculated the power spectral density between 0.5 and 5 Hz in log frequency. Finally, we simultaneously separated the site response ( $S_i$ ) and the earthquake source effect ( $E_j$ ) from the observed spectrum ( $O_{ij}$ ) at channel  $i$  for event  $j$  with a generalized inversion in matrix form as  $Gm = d$  for each frequency (Yang et al., 2022a). The solved site amplification profile is further smoothed with a running spatial window of 400 m and normalized to the channel with the lowest amplification factor.

Figure 14a shows the calculated earthquake spectral amplitude averaged between 0.5 and 5 Hz for every 20-m channel. Most of the local events are located near the DAS array with nearest distances less than 5 km and magnitudes (Mw) around 2 (see Figure S4 in Supporting Information S1 for details of the seismic event distribution). Considering the  $V_s30$  profile is closely tied to soil rigidity, there is no doubt that  $V_s30$  can be a useful proxy for site effect (Castellaro et al., 2008). Borchardt et al. (1978) indicated the anti-correlation relationship between site effect and  $V_s30$  based on a database from the San Francisco Bay Area. To some extent, we can detect some local anti-correlation for lateral variations between the site amplification profile and the estimated  $V_s30$  profile (Figure 14b). However, it is worth noting that the spectrum of the near-line events depicts a clear pattern with a stronger amplitude distributed in the north and a weaker amplitude in the south (Figure 14a). A similar pattern can be observed on the frequency-averaged site effects (see Figure S5 in Supporting Information S1 for the original inverted site amplification for each frequency). This likely suggests that the overdetermined inverse problem of spectral decomposition is not well solved, and that the path effects and/or the source effects might not be effectively separated from the obtained site effect estimates. Note that the sudden drop in site amplification around 15 km (highlighted with the double arrows) is likely caused by the imperfect denoising algorithm, considering the stronger persistent noise sources around this area, particularly for the near-line events.

To avoid uncertainties in site effect inversion and to attenuate effects from the ray path and the earthquake source, we modified the conventional spatial ratio method (Borchardt, 1970) by calculating the ratio between the



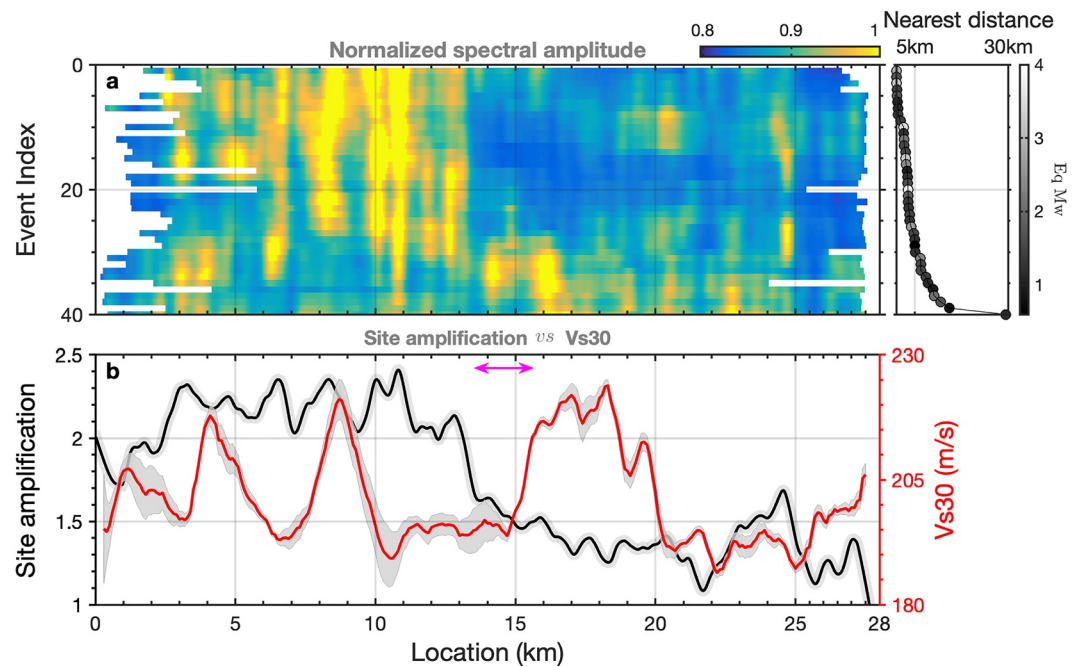


**Figure 14.** Seismic site amplification estimation and its correlation with the obtained  $V_{s30}$  profile. (a) The normalized spectrum of 40 denoised events. The black-white scatters on the side panel show the nearest distances between each event and the DAS line; the colors are coded by the magnitudes. (b) The frequency-averaged (0.5–5 Hz) site amplification profile (black curve, normalized to the channel with the lowest site effect) and the obtained  $V_{s30}$  profile along the cable. The gray patch along the  $V_{s30}$  profile indicates the standard deviation of the obtained  $V_{s30}$  profiles from DAS as shown in Figure 12. The magenta double arrow indicates the locations of the persistent noise sources, as well as the polluted spectrum and site effects.

observed event spectrum and the pre-event noise spectrum, since no bedrock reference site is located along our DAS array. This modified spatial ratio is also known as the spectral SNR of earthquake events in the seismology community (Chen & Shearer, 2011; Shearer et al., 2006). The assumption for using this parameter to approximate site effect is that the amplified ground motions usually show higher SNR considering a relatively uniform ambient noise environment after denoising, and the spectral ratio between the event and the pre-event noise is able to get rid of path effects and source effects. We separated the denoised wavefield into 4 s before and 2 s after the picked S arrivals as the pre-event noise window and the event window, respectively; next we calculated the ratio  $R_{ij}$  between the event spectrum  $S_{ij}(f)$  and the pre-event noise spectrum  $N_{ij}(f)$  at channel  $i$  for event  $j$  with

$$R_{ij} = \frac{\max\{S_{ij}(f)\}}{\text{rms}\{N_{ij}(f)\}} (0.5\text{Hz} < f < 5\text{Hz}). \quad (6)$$

where we calculated the ratio using the peak spectrum of the event and the RMS spectrum of the pre-event noise between 0.5 and 5 Hz to increase the stability of the spectral ratio computation. To focus on lateral variations, we normalized the spectral ratio along the cable. The obtained spectral ratio (Figure 15a) appears generally consistent across different events, which probably benefits from the attenuation of path effects and source effects. To further enhance the pattern of lateral variations, the spectral ratio profiles of all events were averaged together and smoothed with a running spatial window of 400 m. Compared to the inverted site amplification profile, the modified spectral ratio profile (the black curve in Figure 15b) reveals a more pronounced anti-correlation relationship with the  $V_{s30}$  profile (the red curve in Figure 15b). This implies higher site amplification in the south and the middle of our DAS profile, where extra attention should be paid to further strong ground motion monitoring. Note that the sudden drop around 15 km (highlighted with the double arrows in Figure 15b) can also be observed which might be caused by the imperfect denoising as aforementioned. Furthermore, it is challenging to provide a simple quantitative metric to describe the relationship between the estimated site effect and the inverted  $V_{s30}$  profile, because the physical phenomena of site effects are too complex to be captured by a single parameter (Castellaro et al., 2008).

Our preliminary tests indicate that utilizing the modified spectral ratio (Equation 6) is a promising alternative to qualitatively evaluate near-surface site effects in the case where no reference site is available. Attention should be

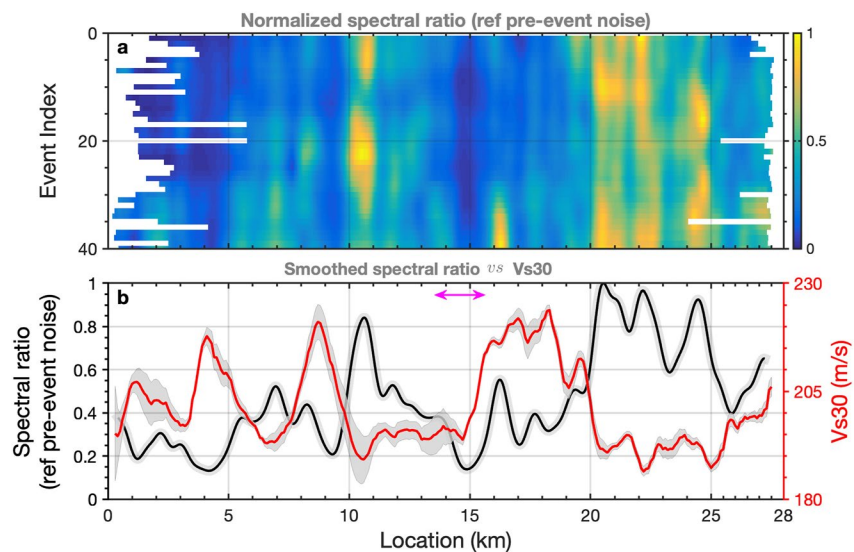


**Figure 15.** Normalized spectral ratio and its correlation with the obtained  $V_{s30}$  profile. (a) The normalized spectral ratio of 40 denoised events. (b) The event-averaged spectral ratio profile and the obtained  $V_{s30}$  profile along the cable.

paid to the inverted site amplifications using the spectrum decomposition technique due to the potential ambiguity in the inverse problem, particularly for the cases where events are broadly distributed at two sides of the survey profile like our case. These preliminary results are limited by the availability of a limited number of low-magnitude local events; more events should be required for our future work, where events with higher magnitudes and less interference are desired.

## 6. Conclusions

We use DAS deployed on existing telecommunication cable to extract high-quality surface waves from ambient noise data and retrieve a 28-km high-resolution S wave velocity model for near-surface site effects estimation in the Imperial Valley. For the first time, we evaluate the performance of three different surface wave dispersion analysis methods (MAPS, SPAC, and ReMi) on DAS ambient noise dispersion imaging. Results indicate that interferometric methods (MAPS and SPAC) show improved resolution for higher overtone evaluation, particularly for the MAPS method, while non-interferometric methods (ReMi) can highlight the trend of the fundamental mode dispersion energy and allow picking of dispersion curves to higher frequencies. This suggests that a combination of various techniques should be considered during DAS surface wave analysis to provide mutual evidence of the accuracy for dispersion measurements. We also develop a quality control workflow to attenuate the non-uniform source effects on the DAS ambient noise data using a selective stacking technique of the  $fk$  domain.

We then jointly invert multiple surface wave modes and obtain a high-resolution  $V_s$  structure, which reveals generally flat basin sediment below 30 m depth overlaid with several soft surface zones; this interpretation has been corroborated by ambient noise autocorrelation profile analysis and USGS downhole velocity surveys. Using two independent techniques, we estimate a  $V_{s30}$  profile at the basin scale (28 km) with a spatial resolution of 100 m, which can be further refined to tens of meters with appropriate subarray length as well as coverage overlap. The  $V_{s30}$  profile shows higher spatial resolution and reliability compared to the model of Thompson et al. (2014), and indicates that DAS is promising for high-resolution near-surface site effect estimation as well as seismic hazard mapping.

With the assistance of a secondary data set, local earthquakes observed on our DAS array, we conduct some preliminary analysis of site effect factors using 40 events. Our preliminary results reveal a clear anti-correlation between the approximated site response and the  $V_{s30}$  profile, as would be expected, and highlight the potential of combining DAS ambient noise and DAS earthquake events for high spatial resolution site response estimation. Our study is a significant step forward since such models were not previously possible from either earthquake ground motion or local geology and terrain.

### Data Availability Statement

The 2-day raw DAS waveforms have been made available through the Department of Energy (DOE) Geothermal Data Repository (GDR): <https://gdr.openei.org/submissions/1499> (Ajo-Franklin et al., 2020). The extracted empirical Green's functions, the inverted shear velocity model used in this work and a small data chunk with 40-min raw DAS waveforms are available in the following OSF repository: <https://osf.io/ckt9q> (Cheng & Ajo-Franklin, 2022). The Geopsy package 3.3.6 used for  $V_s$  inversion is from Wathelet et al. (2004) under the DOI: <https://doi.org/10.1785/0220190360>. The dispersion imaging algorithms used for MAPS, SPAC and ReMi dispersion measurements can be found at <https://github.com/marscfeng/dcImage4ChengIVDF2023> and Zenodo repository (Cheng, 2023). The USGS  $V_s30$  map for California is downloaded from <https://doi.org/10.5066/F7JQ108S> (Thompson et al., 2014). All websites were last accessed in July 2023.

### Acknowledgments

This project was supported by U.S. Department of Energy (DOE) under Award Number DE-AC02-05CH11231 with Lawrence Berkeley National Laboratory (LBNL), Geothermal Technologies Office (GTO), the Office of Energy Efficiency and Renewable Energy (EERE), and the Startup Funds of Zhejiang University. We thank the Imperial Valley Dark Fiber (IVDF) team for efforts on data acquisition and results discussion. The IVDF Team includes Jonathan Ajo-Franklin (Rice University), Feng Cheng (Zhejiang University and Rice University), Verónica Rodríguez Tribaldos (GFZ Potsdam and LBNL), Avinash Nayak (LBNL), Todd Wood (LBNL), Michelle Robertson (LBNL), Kesheng Wu (LBNL), Bin Dong (LBNL), Patrick Dobson (LBNL), Robert Mellors (Scripps Institution of Oceanography), Cody Rotermund (ESnet and LBNL), Benxin Chi (Chinese Academy of Sciences, formerly Rice University); Eric Matzel (LLNL), Dennis C. Templeton (LLNL), Christina Morency (LLNL). We appreciate the useful discussion about spectral decomposition method with Dr. Xiaowei Chen. We thanks Dr. Shengji Wei for providing the information of surface rupture in 2012 Brawley Swarm.

### References

Ajo-Franklin, J., Dobson, P., & Rodríguez Tribaldos, V. (2020). Imperial valley dark fiber project continuous das data [Dataset]. Geothermal Data Repository. Retrieved from <https://gdr.openei.org/submissions/1499>

Ajo-Franklin, J., Dou, S., Lindsey, N., Monga, I., Tracy, C., Robertson, M., et al. (2019). Distributed acoustic sensing using dark fiber for near-surface characterization and broadband seismic event detection. *Scientific Reports*, 9(1), 1–14. <https://doi.org/10.1038/s41598-018-36675-8>

Ajo-Franklin, J., Rodríguez Tribaldos, V., Nayak, A., Cheng, F., Mellors, R., Chi, B., et al. (2022). The imperial valley dark fiber project: Towards seismic studies using DAS and telecom infrastructure for geothermal applications. *Seismological Research Letters*, 93(5), 2906–2919. <https://doi.org/10.1785/0220220072>

Aki, K. (1965). A note on the use of microseisms in determining the shallow structures of the Earth's crust. *Geophysics*, 30(4), 665–666. <https://doi.org/10.1190/1.1439640>

Aki, K. (1993). Local site effects on weak and strong ground motion. *Tectonophysics*, 218(1–3), 93–111. [https://doi.org/10.1016/0040-1951\(93\)90262-i](https://doi.org/10.1016/0040-1951(93)90262-i)

Anderson, J. (2007). Physical processes that control strong ground motion. *Earthquake Seismology*, 4, 513–565.

Andrews, D. (1986). Objective determination of source parameters and similarity of earthquakes of different size. *Earthquake Source Mechanics*, 37, 259–267.

Asten, M. (2006). On bias and noise in passive seismic data from finite circular array data processed using SPAC methods. *Geophysics*, 71(6), 153–162. <https://doi.org/10.1190/1.2345054>

Asten, M., Yong, A., Foti, S., Hayashi, K., Martin, A. J., Stephenson, W. J., et al. (2022). An assessment of uncertainties in VS profiles obtained from microtremor observations in the phased 2018 COSMOS blind trials. *Journal of Seismology*, 26(4), 1–24. <https://doi.org/10.1007/s10950-021-10059-4>

Atterholt, J., Zhan, Z., Shen, Z., & Li, Z. (2022). A unified wavefield-partitioning approach for distributed acoustic sensing. *Geophysical Journal International*, 228(2), 1410–1418. <https://doi.org/10.1093/gji/ggab407>

Behm, M., Cheng, F., Patterson, A., & Soreghan, G. (2019). Passive processing of active nodal seismic data: Estimation of Vp/Vs ratios to characterize structure and hydrology of an alpine valley infill. *Solid Earth*, 1–32. <https://doi.org/10.5194/se-2019-47>

Bensen, G., Ritzwoller, M., Barmin, M., Levshin, A. L., Lin, F., Moschetti, M., et al. (2007). Processing seismic ambient noise data to obtain reliable broad-band surface wave dispersion measurements. *Geophysical Journal International*, 169(3), 1239–1260. <https://doi.org/10.1111/j.1365-246x.2007.03374.x>

Borcherdt, R. D. (1970). Effects of local geology on ground motion near San Francisco Bay. *Bulletin of the Seismological Society of America*, 60(1), 29–61.

Borcherdt, R. D., Gibbs, J. F., & Fumal, T. E. (1978). Progress on ground motion predictions for the San Francisco Bay region, California. In *Proceedings of 2nd international conference on microzonation* (pp. 241–253).

Brown, L., Diehl, J. G., & Nigbor, R. L. (2000). A simplified procedure to measure average shear-wave velocity to a depth of 30 meters ( $V_s30$ ). In *Proceedings of 12th world conference on earthquake engineering* (pp. 1–8).

Campillo, M., & Paul, A. (2003). Long-range correlations in the diffuse seismic coda. *Science*, 299(5606), 547–549. <https://doi.org/10.1126/science.1078551>

Castellanos, J. C., & Clayton, R. (2021). The fine-scale structure of Long Beach, California, and its impact on ground motion acceleration. *Journal of Geophysical Research: Solid Earth*, 126(12), e2021JB022462. <https://doi.org/10.1029/2021jb022462>

Castellanos, J. C., Clayton, R., & Juarez, A. (2020). Using a time-based subarray method to extract and invert noise-derived body waves at Long Beach, California. *Journal of Geophysical Research: Solid Earth*, 125(5), e2019JB018855. <https://doi.org/10.1029/2019jb018855>

Castellano, S., Mulargia, F., & Rossi, P. L. (2008). VS30: Proxy for seismic amplification? *Seismological Research Letters*, 79(4), 540–543. <https://doi.org/10.1785/gssrl.79.4.540>

Chávez-García, F. J., Rodríguez, M., & Stephenson, W. R. (2006). Subsoil structure using SPAC measurements along a line. *Bulletin of the Seismological Society of America*, 96(2), 729–736. <https://doi.org/10.1785/0120050141>

Chen, X. (2023). Source parameter analysis using distributed acoustic sensing—An example with the PoroTomo array. *Geophysical Journal International*, 233(3), 2207–2213. <https://doi.org/10.1093/gji/ggad061>

Chen, X., & Shearer, P. (2011). Comprehensive analysis of earthquake source spectra and swarms in the Salton Trough, California. *Journal of Geophysical Research*, 116(B9), B09309. <https://doi.org/10.1029/2011jb008263>

Chen, X., Xia, J., Pang, J., Zhou, C., & Mi, B. (2022). Deep learning inversion of Rayleigh-wave dispersion curves with geological constraints for near-surface investigations. *Geophysical Journal International*, 231(1), 1–14. <https://doi.org/10.1093/gji/ggac171>

Cheng, F. (2023). dcimage4chengivdf2023: July 22, 2023 release (version 0) [Software]. Zenodo. <https://doi.org/10.5281/zenodo.8173925>

Cheng, F., & Ajo-Franklin, J. (2022). Imperial valley dark fiber project continuous das data part 2 [Dataset]. Open Science Framework. <https://osf.io/ckt9q>

Cheng, F., Ajo-Franklin, J., Nayak, A., Rodríguez Tribaldos, V., Mellors, R., Dobson, P., & Imperial Valley Dark Fiber Team. (2023a). Using dark fiber and distributed acoustic sensing to characterize a geothermal system in the imperial valley, southern California. *Journal of Geophysical Research: Solid Earth*, 128(3), e2022JB025240. <https://doi.org/10.1029/2022JB025240>

Cheng, F., Xia, J., Luo, Y., Xu, Z., Wang, L., Shen, C., et al. (2016). Multi-channel analysis of passive surface waves based on cross-correlations. *Geophysics*, 81(5), EN57–EN66. <https://doi.org/10.1190/geo2015-0505.1>

- Cheng, F., Xia, J., Xu, Z., & Ajo-Franklin, J. B. (2023b). Comparisons between non-interferometric and interferometric passive surface wave imaging methods—Towards linear receiver array. *Geophysical Journal International*, 233(1), 680–690. <https://doi.org/10.1093/gji/ggac475>
- Cheng, F., Xia, J., Xu, Z., Hu, Y., & Mi, B. (2018). Frequency-wavenumber (FK)-based data selection in high-frequency passive surface wave survey. *Surveys in Geophysics*, 39(4), 661–682. <https://doi.org/10.1007/s10712-018-9473-3>
- Cheng, F., Xia, J., Zhang, K., Zhou, C., & Ajo-Franklin, J. B. (2021). Phase-weighted slant-stacking for surface wave dispersion measurement. *Geophysical Journal International*, 226(1), 256–269. <https://doi.org/10.1093/gji/ggab101>
- Clayton, C. R. (1995). *The standard penetration test (SPT): Methods and use*. Construction Industry Research and Information Association.
- Clayton, R. W. (2020). Imaging the subsurface with ambient noise autocorrelations. *Seismological Research Letters*, 91(2), 4852–4856. <https://doi.org/10.1785/0220190272>
- Clayton, R., Persaud, P., Denolle, M., & Polet, J. (2019). Exposing Los Angeles's shaky geologic underbelly. *Eos*, 100. <https://doi.org/10.1029/2019eo135099>
- Dai, T., Xia, J., Ning, L., Xi, C., Liu, Y., & Xing, H. (2021). Deep learning for extracting dispersion curves. *Surveys in Geophysics*, 42(1), 69–95. <https://doi.org/10.1007/s10712-020-09615-3>
- Daley, T. M., Freifeld, B. M., Ajo-Franklin, J., Dou, S., Pevzner, R., Shulakova, V., et al. (2013). Field testing of fiber-optic distributed acoustic sensing (DAS) for subsurface seismic monitoring. *The Leading Edge*, 32(6), 699–706. <https://doi.org/10.1190/le32060699.1>
- Deng, S., & Levander, A. (2020). Autocorrelation reflectivity of Mars. *Geophysical Research Letters*, 47(16), e2020GL089630. <https://doi.org/10.1029/2020GL089630>
- Dobry, R., Borcherdt, R., Crouse, C., Idriss, I., Joyner, W., Martin, G. R., et al. (2000). New site coefficients and site classification system used in recent building seismic code provisions. *Earthquake Spectra*, 16(1), 41–67. <https://doi.org/10.1193/1.1586082>
- Dou, S., Lindsey, N., Wagner, A., Daley, T., Freifeld, B., Robertson, M., et al. (2017). Distributed acoustic sensing for seismic monitoring of the near surface: A traffic-noise interferometry case study. *Scientific Reports*, 7(1), 1–12. <https://doi.org/10.1038/s41598-017-11986-4>
- Ely, G. P., Jordan, T., Small, P., & Maechling, P. J. (2010). A Vs30-derived near-surface seismic velocity model. In *Abstract S51A-1907, fall meeting*.
- Fang, G., Li, Y. E., Zhao, Y., & Martin, E. R. (2020). Urban near-surface seismic monitoring using distributed acoustic sensing. *Geophysical Research Letters*, 47(6), e2019GL086115. <https://doi.org/10.1029/2019gl086115>
- Forbriger, T. (2003). Inversion of shallow-seismic wavefields: I. Wavefield transformation. *Geophysical Journal International*, 153(3), 719–734. <https://doi.org/10.1046/j.1365-246X.2003.01929.x>
- Foti, S., Hollender, F., Garofalo, F., Albarello, D., Asten, M., Bard, P.-Y., et al. (2018). Guidelines for the good practice of surface wave analysis: A product of the InterPACIFIC project. *Bulletin of Earthquake Engineering*, 16(6), 2367–2420. <https://doi.org/10.1007/s10518-017-0206-7>
- Garofalo, F., Foti, S., Hollender, F., Bard, P., Cornou, C., Cox, B., et al. (2016). InterPACIFIC project: Comparison of invasive and non-invasive methods for seismic site characterization. Part II: Inter-comparison between surface-wave and borehole methods. *Soil Dynamics and Earthquake Engineering*, 82, 241–254. <https://doi.org/10.1016/j.soildyn.2015.12.009>
- Hauksson, E., Stock, J., Bilham, R., Boese, M., Chen, X., Fielding, E. J., et al. (2013). Report on the august 2012 Brawley earthquake swarm in imperial valley, southern California. *Seismological Research Letters*, 84(2), 177–189. <https://doi.org/10.1785/0220120169>
- Hauksson, E., Yang, W., & Shearer, P. M. (2012). Waveform relocated earthquake catalog for southern California (1981 to June 2011). *Bulletin of the Seismological Society of America*, 102(5), 2239–2244. <https://doi.org/10.1785/0120120010>
- Hayashi, K., Asten, M., Stephenson, W. J., Cornou, C., Hobiger, M., Pilz, M., & Yamanaka, H. (2022). Microtremor array method using spatial autocorrelation analysis of Rayleigh-wave data. *Journal of Seismology*, 26(4), 1–27. <https://doi.org/10.1007/s10950-021-10051-y>
- Henderson, D. J., & Parmeter, C. F. (2015). *Applied nonparametric econometrics*. Cambridge University Press.
- Hu, S., Luo, S., & Yao, H. (2020). The frequency-Bessel spectrograms of multicomponent cross-correlation functions from seismic ambient noise. *Journal of Geophysical Research: Solid Earth*, 125(8), e2020JB019630. <https://doi.org/10.1029/2020jb019630>
- Imtiaz, A., Perron, V., Hollender, F., Bard, P.-Y., Cornou, C., Svay, A., & Theodoulidis, N. (2018). Wavefield characteristics and spatial incoherence: A comparative study from Argostoli rock-and soil-site dense seismic arrays wavefield characteristics and spatial incoherence. *Bulletin of the Seismological Society of America*, 108(5A), 2839–2853. <https://doi.org/10.1785/0120180025>
- James, S., Knox, H., Abbott, R., Panning, M., & Screation, E. (2019). Insights into permafrost and seasonal active-layer dynamics from ambient seismic noise monitoring. *Journal of Geophysical Research: Earth Surface*, 124(7), 1798–1816. <https://doi.org/10.1029/2019jfo005051>
- Johnson, C. E., & Hadley, D. M. (1976). Tectonic implications of the Brawley earthquake swarm, imperial valley, California, January 1975. *Bulletin of the Seismological Society of America*, 66(4), 1133–1144.
- Jousset, P., Currenti, G., Schwarz, B., Chalari, A., Tilmann, F., Reinsch, T., et al. (2022). Fibre optic distributed acoustic sensing of volcanic events. *Nature Communications*, 13(1), 1753. <https://doi.org/10.1038/s41467-022-29184-w>
- Kagami, H., Duke, C. M., Liang, G. C., & Ohta, Y. (1982). Observation of 1- to 5-second microtremors and their application to earthquake engineering. Part II. Evaluation of site effect upon seismic wave amplification due to extremely deep soil deposits. *Bulletin of the Seismological Society of America*, 72(3), 987–998. <https://doi.org/10.1785/BSSA0720030987>
- Kagami, H., Okada, S., Shiono, K., Oner, M., Dravinski, M., & Mal, A. K. (1986). Observation of 1- to 5-second microtremors and their application to earthquake engineering. Part III. A two-dimensional study of site effects in the San Fernando Valley. *Bulletin of the Seismological Society of America*, 76(6), 1801–1812. <https://doi.org/10.1785/BSSA0760061801>
- Kaspareit, D., Mann, M., Sanyal, S., Rickard, B., Osborn, W., & Hulen, J. (2016). Updated conceptual model and reserve estimate for the Salton Sea geothermal field, Imperial Valley, California. *Geothermal Resources Council—Transactions*, 40, 57–66.
- Kawase, H. (1996). The cause of the damage belt in Kobe: “The basin-edge effect,” constructive interference of the direct S-wave with the basin-induced diffracted/Rayleigh waves. *Seismological Research Letters*, 67(5), 25–34. <https://doi.org/10.1785/gssrl.67.5.25>
- Kita, T., Hayashi, K., & Bingol, H. (2011). The development of a 2-dimensional microtremor survey method based on SPAC method using sequential linear arrays. In *24rd EEGS symposium on the application of geophysics to engineering and environmental problems* (pp. cp–247).
- Lehuteur, M., Vergne, J., Maggi, A., & Schmittbuhl, J. (2016). Ambient noise tomography with non-uniform noise sources and low aperture networks: Case study of deep geothermal reservoirs in northern Alsace, France. *Geophysical Supplements to the Monthly Notices of the Royal Astronomical Society*, 208(1), 193–210. <https://doi.org/10.1093/gji/ggw373>
- Lepore, S., & Grad, M. (2020). Relation between ocean wave activity and wavefield of the ambient noise recorded in northern Poland. *Journal of Seismology*, 24(6), 1075–1094. <https://doi.org/10.1007/s10950-020-09963-y>
- Li, J., Feng, Z., & Schuster, G. (2017). Wave-equation dispersion inversion. *Geophysical Journal International*, 208(3), 1567–1578. <https://doi.org/10.1093/gji/ggw465>
- Lin, F.-C., Moschetti, M. P., & Ritzwoller, M. H. (2008). Surface wave tomography of the western United States from ambient seismic noise: Rayleigh and love wave phase velocity maps. *Geophysical Journal International*, 173(1), 281–298. <https://doi.org/10.1111/j.1365-246X.2008.03720.x>

- Lin, F.-C., Ritzwoller, M. H., & Snieder, R. (2009). Eikonal tomography: Surface wave tomography by phase front tracking across a regional broad-band seismic array. *Geophysical Journal International*, 177(3), 1091–1110. <https://doi.org/10.1111/j.1365-246x.2009.04105.x>
- Lin, S., & Ashlock, J. C. (2014). Multimode Rayleigh wave profiling by hybrid surface and borehole methods. *Geophysical Journal International*, 197(2), 1184–1195. <https://doi.org/10.1093/gji/ggu051>
- Lin, S., Gucunski, N., Shams, S., & Wang, Y. (2021). Seismic site classification from surface wave data to  $V_{s,30}$  without inversion. *Journal of Geotechnical and Geoenvironmental Engineering*, 147(6), 04021029. [https://doi.org/10.1061/\(asce\)gt.1943-5606.0002526](https://doi.org/10.1061/(asce)gt.1943-5606.0002526)
- Lindsey, N. J., Martin, E. R., Dreger, D. S., Freifeld, B., Cole, S., James, S. R., et al. (2017). Fiber-optic network observations of earthquake wavefields. *Geophysical Research Letters*, 44(23), 11–792. <https://doi.org/10.1002/2017gl075722>
- Liu, H., Li, J., & Wang, Y. (2022). Wave equation dispersion inversion of distributed acoustic sensing data. *Journal of Geophysical Research: Solid Earth*, 127(11), e2022JB024671. <https://doi.org/10.1029/2022JB024671>
- Liu, Y., Xia, J., Cheng, F., Xi, C., Shen, C., & Zhou, C. (2020). Pseudo-linear-array analysis of passive surface waves based on beamforming. *Geophysical Journal International*, 221(1), 640–650. <https://doi.org/10.1093/gji/ggaa024>
- Liu, Y., Xia, J., Xi, C., Dai, T., & Ning, L. (2021). Improving the retrieval of high-frequency surface waves from ambient noise through multichannel-coherency-weighted stack. *Geophysical Journal International*, 227(2), 776–785. <https://doi.org/10.1093/gji/ggab253>
- Lohman, R., & McGuire, J. (2007). Earthquake swarms driven by aseismic creep in the Salton Trough, California. *Journal of Geophysical Research*, 112(B4). <https://doi.org/10.1029/2006jb004596>
- Louie, J. N. (2001). Faster, better: Shear-wave velocity to 100 meters depth from refraction microtremor arrays. *Bulletin of the Seismological Society of America*, 91(2), 347–364. <https://doi.org/10.1785/0120000098>
- Louie, J. N., Pancha, A., & Kissane, B. (2021). Guidelines and pitfalls of refraction microtremor surveys. *Journal of Seismology*, 26(4), 1–16. <https://doi.org/10.1007/s10950-021-10020-5>
- Maechling, P. J., Su, M.-H., Plesch, A., Shaw, J. H., & Callaghan, S. (2019). New capabilities of the SCEC unified community velocity model (UCVM) software framework. In *AGU fall meeting abstracts* (Vol. 2019, pp. NS21A–17).
- Mao, S., Lecointre, A., van der Hilst, R. D., & Campillo, M. (2022). Space-time monitoring of groundwater fluctuations with passive seismic interferometry. *Nature Communications*, 13(1), 4643. <https://doi.org/10.1038/s41467-022-32194-3>
- Margaryan, S., Yokoi, T., & Hayashi, K. (2009). Experiments on the stability of the spatial autocorrelation method (SPAC) and linear array methods and on the imaginary part of the SPAC coefficients as an indicator of data quality. *Exploration Geophysics*, 40(1), 121–131. <https://doi.org/10.1071/eg08101>
- Martins, J. E., Weemstra, C., Ruigrok, E., Verdel, A., Jousset, P., & Hersir, G. (2020). 3D S-wave velocity imaging of Reykjanes Peninsula high-enthalpy geothermal fields with ambient-noise tomography. *Journal of Volcanology and Geothermal Research*, 391, 106685. <https://doi.org/10.1016/j.jvolgeores.2019.106685>
- McPhillips, D., Herrick, J., Ahdi, S., Yong, A., & Haefner, S. (2020). Updated compilation of VS30 data for the United States: US geological survey data release.
- Mi, B., Xia, J., Tian, G., Shi, Z., Xing, H., Chang, X., et al. (2022). Near-surface imaging from traffic-induced surface waves with dense linear arrays: An application in the urban area of Hangzhou, China. *Geophysics*, 87(2), B145–B158. <https://doi.org/10.1190/geo2021-0184.1>
- Muffler, L. P., & White, D. E. (1969). Active metamorphism of upper Cenozoic sediments in the Salton Sea geothermal field and the Salton Trough, southeastern California. *Geological Society of America Bulletin*, 80(2), 157–181. [https://doi.org/10.1130/0016-7606\(1969\)80\[157:amoucs\]2.0.co;2](https://doi.org/10.1130/0016-7606(1969)80[157:amoucs]2.0.co;2)
- Nakamura, Y. (1989). *A method for dynamic characteristics estimation of subsurface using microtremor on the ground surface* (Vol. 30). Railway Technical Research Institute, Quarterly Reports.
- Nakamura, Y. (2019). *What is the Nakamura method?* Seismological Society of America.
- Nakata, N., Chang, J. P., Lawrence, J. F., & Boué, P. (2015). Body wave extraction and tomography at Long Beach, California, with ambient-noise interferometry. *Journal of Geophysical Research: Solid Earth*, 120(2), 1159–1173. <https://doi.org/10.1002/2015JB011870>
- Nakata, N., & Snieder, R. (2014). Monitoring a building using deconvolution interferometry. II: Ambient-vibration analysis monitoring a building using deconvolution interferometry. II: Ambient-vibration analysis. *Bulletin of the Seismological Society of America*, 104(1), 204–213. <https://doi.org/10.1785/0120130050>
- Nakata, N., Snieder, R., Tsuji, T., Larner, K., & Matsuoka, T. (2011). Shear wave imaging from traffic noise using seismic interferometry by cross-coherence. *Geophysics*, 76(6), SA97–SA106. <https://doi.org/10.1190/geo2010-0188.1>
- Nayak, A., Ajo-Franklin, J., & The Imperial Valley Dark Fiber Team. (2021). Measurement of surface-wave phase-velocity dispersion on mixed inertial seismometer–distributed acoustic sensing seismic noise cross-correlations. *Bulletin of the Seismological Society of America*, 111(6), 3432–3450. <https://doi.org/10.1785/0120210028>
- Nazarian, S., Stokoe, K. H., II., & Hudson, W. R. (1983). *Use of spectral analysis of surface waves method for determination of moduli and thicknesses of pavement systems* (Vol. 930). Transportation Research Record.
- Okada, H., & Suto, K. (2003). *The microtremor survey method*. Society of Exploration Geophysicists.
- O'Neill, A., & Matsuoka, T. (2005). Dominant higher surface-wave modes and possible inversion pitfalls. *Journal of Environmental & Engineering Geophysics*, 10(2), 185–201. <https://doi.org/10.2113/jeeeg10.2.185>
- Oren, C., & Nowack, R. L. (2016). Seismic body-wave interferometry using noise auto-correlations for crustal structure. *Geophysical Journal International*, 208(1), ggw394–332. <https://doi.org/10.1093/gji/ggw394>
- Pan, Y., Xia, J., Xu, Y., Xu, Z., Cheng, F., Xu, H., & Gao, L. (2016). Delineating shallow S-wave velocity structure using multiple ambient-noise surface-wave methods: An example from western Junggar, China. *Bulletin of the Seismological Society of America*, 106(2), 327–336. <https://doi.org/10.1785/0120150014>
- Pancha, A., Anderson, J. G., Louie, J. N., & Pullammanappallil, S. K. (2008). Measurement of shallow shear wave velocities at a rock site using the ReMi technique. *Soil Dynamics and Earthquake Engineering*, 28(7), 522–535. <https://doi.org/10.1016/j.soildyn.2007.08.005>
- Pang, J., Cheng, F., Shen, C., Dai, T., Ning, L., & Zhang, K. (2019). Automatic passive data selection in time domain for imaging near-surface surface waves. *Journal of Applied Geophysics*, 162, 108–117. <https://doi.org/10.1016/j.jappgeo.2018.12.018>
- Park, C., Miller, R., Laflen, D., Neb, C., Ivanov, J., Bennett, B., & Huggins, R. (2004). Imaging dispersion curves of passive surface waves. In *SEG technical program expanded abstracts 2004* (pp. 1357–1360). Society of Exploration Geophysicists.
- Park, C. B. (2005). *MASW horizontal resolution in 2D shear-velocity (Vs) mapping*. Open-File Report (Vol. 36). Kansas Geologic Survey. Retrieved from <http://www.masw.com/files/KGS-05-04.pdf>
- Park, C. B., & Miller, R. D. (2008). Roadside passive multichannel analysis of surface waves (MASW). *Journal of Environmental & Engineering Geophysics*, 13(NO.1), 1–11. <https://doi.org/10.2113/jeeeg13.1.1>
- Park, C. B., Miller, R. D., & Xia, J. (1999). Multichannel analysis of surface waves. *Geophysics*, 64(3), 800–808. <https://doi.org/10.1190/1.1444590>

- Perron, V., Gélis, C., Froment, B., Hollender, F., Bard, P.-Y., Cultrera, G., & Cushing, E. M. (2018). Can broad-band earthquake site responses be predicted by the ambient noise spectral ratio? Insight from observations at two sedimentary basins. *Geophysical Journal International*, 215(2), 1442–1454. <https://doi.org/10.1093/gji/ggy355>
- Planès, T., Obermann, A., Antunes, V., & Lupi, M. (2020). Ambient-noise tomography of the Greater Geneva Basin in a geothermal exploration context. *Geophysical Journal International*, 220(1), 370–383. <https://doi.org/10.1093/gji/ggz457>
- Porcella, R. L. (1984). *Geotechnical investigations at strong-motion stations in the imperial valley, California*. (Technical Report). US Department of the Interior, Geological Survey. Retrieved from <https://pubs.usgs.gov/of/1984/0562/report.pdf>
- Sager, K., Ermert, L., Boehm, C., & Fichtner, A. (2018). Towards full waveform ambient noise inversion. *Geophysical Journal International*, 212(1), 566–590. <https://doi.org/10.1093/gji/ggx429>
- Schimmel, M., Stutzmann, E., & Gallart, J. (2011). Using instantaneous phase coherence for signal extraction from ambient noise data at a local to a global scale. *Geophysical Journal International*, 184(1), 494–506. <https://doi.org/10.1111/j.1365-246x.2010.04861.x>
- Shapiro, N. M., & Campillo, M. (2004). Emergence of broadband Rayleigh waves from correlations of the ambient seismic noise. *Geophysical Research Letters*, 31(7), L07614. <https://doi.org/10.1029/2004gl019491>
- Shearer, P. M., Prieto, G. A., & Hauksson, E. (2006). Comprehensive analysis of earthquake source spectra in southern California. *Journal of Geophysical Research*, 111(B6), B06303. <https://doi.org/10.1029/2005jb003979>
- Snieder, R. (2004). Extracting the Green's function from the correlation of coda waves: A derivation based on stationary phase. *Physical Review E*, 69(4), 046610. <https://doi.org/10.1103/physreve.69.046610>
- Snieder, R., Miyazawa, M., Slob, E., Vasconcelos, I., & Wapenaar, K. (2009). A comparison of strategies for seismic interferometry. *Surveys in Geophysics*, 30(4–5), 503–523. <https://doi.org/10.1007/s10712-009-9069-z>
- Socco, L. V., Foti, S., & Boiero, D. (2010). Surface-wave analysis for building near-surface velocity models—Established approaches and new perspectives. *Geophysics*, 75(5), 75A83–75A102. <https://doi.org/10.1190/1.3479491>
- Solomon, O., Larson, D. R., & Paulter, N. (2001). Comparison of some algorithms to estimate the low and high state level of pulses. In *IMTC 2001. Proceedings of the 18th IEEE instrumentation and measurement technology conference* (Vol. 1, pp. 96–101). Rediscovering measurement in the age of informatics (cat. no. 01ch 37188).
- Song, Y.-Y., Castagna, J. P., Black, R. A., & Knapp, R. W. (1989). Sensitivity of near-surface shear-wave velocity determination from Rayleigh and love waves. In *SEG technical program expanded abstracts 1989* (pp. 509–512). Society of Exploration Geophysicists.
- Spica, Z. J., Nishida, K., Akuhara, T., Pétrélis, F., Shinohara, M., & Yamada, T. (2020a). Marine sediment characterized by ocean-bottom fiber-optic seismology. *Geophysical Research Letters*, 47(16), 1–10. <https://doi.org/10.1029/2020GL088360>
- Spica, Z. J., Perton, M., Martin, E. R., Beroza, G. C., & Biondi, B. (2020b). Urban seismic site characterization by fiber-optic seismology. *Journal of Geophysical Research: Solid Earth*, 125(3), e2019JB018656. <https://doi.org/10.1029/2019jb018656>
- Stokoe, K. I., & Nazarian, S. (1983). Effectiveness of ground improvement from spectral analysis of surface waves. In *Proceeding of the eighth European conference on soil mechanics and foundation engineering*.
- Svay, A., Perron, V., Imtiaz, A., Zentner, I., Cottreau, R., Clouteau, D., et al. (2017). Spatial coherency analysis of seismic ground motions from a rock site dense array implemented during the Kefalonia 2014 aftershock sequence. *Earthquake Engineering & Structural Dynamics*, 46(12), 1895–1917.
- Thompson, E. (2018). *An updated Vs30 map for California with geologic and topographic constraints*. (Technical Report). US Geological Survey Data Release. <https://doi.org/10.5066/F7JQ108S>
- Thompson, E., Wald, D. J., & Worden, C. (2014). A Vs30 map for California with geologic and topographic constraints Vs30 map for California with geologic and topographic constraints. *Bulletin of the Seismological Society of America*, 104(5), 2313–2321. <https://doi.org/10.1785/0120130312>
- Vantassel, J. P., & Cox, B. R. (2021). A procedure for developing uncertainty-consistent vs profiles from inversion of surface wave dispersion data. *Soil Dynamics and Earthquake Engineering*, 145, 106622. <https://doi.org/10.1016/j.soildyn.2021.106622>
- Walter, F., Gräff, D., Lindner, F., Paitz, P., Köpfl, M., Chmiel, M., & Fichtner, A. (2020). Distributed acoustic sensing of microseismic sources and wave propagation in glaciated terrain. *Nature Communications*, 11(1), 1–10. <https://doi.org/10.1038/s41467-020-15824-6>
- Wang, H. F., Zeng, X., Miller, D. E., Fratta, D., Feigl, K. L., Thurber, C. H., & Mellors, R. J. (2018). Ground motion response to an ml 4.3 earthquake using co-located distributed acoustic sensing and seismometer arrays. *Geophysical Journal International*, 213(3), 2020–2036. <https://doi.org/10.1093/gji/ggy102>
- Wang, H.-Y., & Wang, S.-Y. (2015). A new method for estimating vs (30) from a shallow shear-wave velocity profile (depth < 30 m). *Bulletin of the Seismological Society of America*, 105(3), 1359–1370. <https://doi.org/10.1785/0120140103>
- Wang, J., Wu, G., & Chen, X. (2019). Frequency-Bessel transform method for effective imaging of higher-mode Rayleigh dispersion curves from ambient seismic noise data. *Journal of Geophysical Research: Solid Earth*, 124(4), 3708–3723. <https://doi.org/10.1029/2018JB016595>
- Wang, K., Yang, Y., Jiang, C., Wang, Y., Tong, P., Liu, T., & Liu, Q. (2021). Adjoint tomography of ambient noise data and teleseismic P waves: Methodology and applications to Central California. *Journal of Geophysical Research: Solid Earth*, 126(6), e2021JB021648. <https://doi.org/10.1029/2021JB021648>
- Wang, W., Chen, P., Keifer, I., & Dueker, K. (2017). Full-3D waveform inversion with near-surface ambient-noise data based on discontinuous Galerkin method. In *SEG technical program expanded abstracts 2017* (pp. 1394–1399). Society of Exploration Geophysicists. <https://doi.org/10.1190/segam2017-17795899.1>
- Wapenaar, K. (2004). Retrieving the elastodynamic Green's function of an arbitrary inhomogeneous medium by cross correlation. *Physical Review Letters*, 93(25), 254301. <https://doi.org/10.1103/physrevlett.93.254301>
- Warrick, R. E. (1974). Seismic investigation of a San Francisco Bay mud site. *Bulletin of the Seismological Society of America*, 64(2), 375–385. <https://doi.org/10.1785/bssa0640020375>
- Wathelet, M., Jongmans, D., & Ohrnberger, M. (2004). Surface-wave inversion using a direct search algorithm and its application to ambient vibration measurements. *Near Surface Geophysics*, 2(4), 211–221. <https://doi.org/10.3997/1873-0604.2004018>
- Wei, S., Avouac, J.-P., Hudnut, K. W., Donnellan, A., Parker, J. W., Graves, R. W., et al. (2015). The 2012 Brawley swarm triggered by injection-induced aseismic slip. *Earth and Planetary Science Letters*, 422, 115–125. <https://doi.org/10.1016/j.epsl.2015.03.054>
- Wills, C., & Clahan, K. (2006). Developing a map of geologically defined site-condition categories for California. *Bulletin of the Seismological Society of America*, 96(4A), 1483–1501. <https://doi.org/10.1785/0120050179>
- Wills, C., Gutierrez, C., Perez, F., & Branum, D. (2015). A next generation Vs30 map for California based on geology and topography next generation Vs30 map for California based on geology and topography. *Bulletin of the Seismological Society of America*, 105(6), 3083–3091. <https://doi.org/10.1785/0120150105>
- Winker, C. D. (1987). *Neogene stratigraphy of the Fish Creek-Vallecito section, southern California: Implications for early history of the northern Gulf of California and Colorado delta (San Andreas Fault)*. The University of Arizona.

- Xi, C., Xia, J., Mi, B., Dai, T., Liu, Y., & Ning, L. (2021). Modified frequency–Bessel transform method for dispersion imaging of Rayleigh waves from ambient seismic noise. *Geophysical Journal International*, 225(2), 1271–1280. <https://doi.org/10.1093/gji/ggab008>
- Xia, J., Miller, R. D., & Park, C. B. (1999). Estimation of near-surface shear-wave velocity by inversion of Rayleigh waves. *Geophysics*, 64(3), 691–700. <https://doi.org/10.1190/1.1444578>
- Xia, J., Miller, R. D., Park, C. B., & Tian, G. (2003). Inversion of high frequency surface waves with fundamental and higher modes. *Journal of Applied Geophysics*, 52(1), 45–57. [https://doi.org/10.1016/s0926-9851\(02\)00239-2](https://doi.org/10.1016/s0926-9851(02)00239-2)
- Xia, J., Miller, R. D., Xu, Y., Luo, Y., Chen, C., Liu, J., et al. (2009). High-frequency Rayleigh-wave method. *Journal of Earth Sciences*, 20(3), 563–579. <https://doi.org/10.1007/s12583-009-0047-7>
- Xia, J., Xu, Y., Chen, C., Kaufmann, R. D., & Luo, Y. (2006). Simple equations guide high-frequency surface-wave investigation techniques. *Soil Dynamics and Earthquake Engineering*, 26(5), 395–403. <https://doi.org/10.1016/j.soildyn.2005.11.001>
- Xie, J., Yang, Y., & Luo, Y. (2020). Improving cross-correlations of ambient noise using an RMS-ratio selection stacking method. *Geophysical Journal International*, 222(2), 989–1002. <https://doi.org/10.1093/gji/ggaa232>
- Yan, Y., Chen, X., Huai, N., & Guan, J. (2022). Modern inversion workflow of the multimodal surface wave dispersion curves: Staging strategy and pattern search with embedded Kuhn–Munkres algorithm. *Geophysical Journal International*, 231(1), 47–71. <https://doi.org/10.1093/gji/ggac178>
- Yang, Y., Atterholt, J. W., Shen, Z., Muir, J. B., Williams, E. F., & Zhan, Z. (2022a). Sub-kilometer correlation between near-surface structure and ground motion measured with distributed acoustic sensing. *Geophysical Research Letters*, 49(1), e2021GL096503. <https://doi.org/10.1029/2021gl096503>
- Yang, Y., Zhan, Z., Shen, Z., & Atterholt, J. (2022b). Fault zone imaging with distributed acoustic sensing: Surface-to-surface wave scattering. *Journal of Geophysical Research: Solid Earth*, 127(6), e2022JB024329. <https://doi.org/10.1029/2022jb024329>
- Yao, H., & van der Hilst, R. D. (2009). Analysis of ambient noise energy distribution and phase velocity bias in ambient noise tomography, with application to SE Tibet. *Geophysical Journal International*, 179(2), 1113–1132. <https://doi.org/10.1111/j.1365-246x.2009.04329.x>
- Yu, C., Zhan, Z., Lindsey, N. J., Ajo-Franklin, J. B., & Robertson, M. (2019). The potential of das in teleseismic studies: Insights from the gold-stone experiment. *Geophysical Research Letters*, 46(3), 1320–1328. <https://doi.org/10.1029/2018gl081195>
- Zhan, Z. (2020). Distributed acoustic sensing turns fiber-optic cables into sensitive seismic antennas. *Seismological Research Letters*, 91(1), 1–15. <https://doi.org/10.1785/0220190112>
- Zhang, C., Yao, H., Liu, Q., Zhang, P., Yuan, Y. O., Feng, J., & Fang, L. (2018). Linear array ambient noise adjoint tomography reveals intense crust-mantle interactions in North China Craton. *Journal of Geophysical Research: Solid Earth*, 123(1), 368–383. <https://doi.org/10.1002/2017JB015019>
- Zhou, C., Xi, C., Pang, J., & Liu, Y. (2018). Ambient noise data selection based on the asymmetry of cross-correlation functions for near surface applications. *Journal of Applied Geophysics*, 159, 803–813. <https://doi.org/10.1016/j.jappgeo.2018.09.033>
- Zhu, T., Shen, J., & Martin, E. R. (2021). Sensing earth and environment dynamics by telecommunication fiber-optic sensors: An urban experiment in Pennsylvania, USA. *Solid Earth*, 12(1), 219–235. <https://doi.org/10.5194/se-12-219-2021>